Autophagy

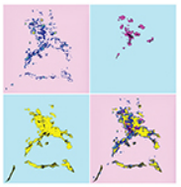

Autophagy

ISSN: 1554-8627 (Print) 1554-8635 (Online) Journal homepage: www.tandfonline.com/journals/kaup20

RAPSN/rapsyn aggregation-induced HSPA/HSP70-BAG3 aggrephagy maintains CHRN integrity in myasthenia gravis

Yujia Liu , Guofang Xia , Huaiying Shi , Simeng Zhu , Hailong Li , Yifan Shi , Wanling Ouyang , Congfeng Xu & Ailian Du

To cite this article: Yujia Liu , Guofang Xia , Huaiying Shi , Simeng Zhu , Hailong Li , Yifan Shi , Wanling Ouyang , Congfeng Xu & Ailian Du (2026) RAPSN/rapsyn aggregation-induced HSPA/HSP70-BAG3 aggrephagy maintains CHRN integrity in myasthenia gravis, Autophagy, 22:11, 3284-3300, DOI: 10.1080/15548627.2026.2693778

To link to this article: https://doi.org/10.1080/15548627.2026.2693778

© 2026 The Author(s). Published by Informa UK Limited, trading as Taylor & Francis Group.

View supplementary material

Published online: 28 Jun 2026.

Submit your article to this journal

Article views: 1017

View related articles

View Crossmark data

Full Terms & Conditions of access and use can be found at
https://www.tandfonline.com/action/journalInformation?journalCode=kaup20

AUTOPHAGY
2026, VOL. 22, NO. 11, 3284–3300
https://doi.org/10.1080/15548627.2026.2693778

Taylor & Francis
by informa

RESEARCH PAPER

OPEN ACCESS Check for updates

RAPSN/rapsyn aggregation-induced HSPA/HSP70-BAG3 aggrephagy maintains CHRN integrity in myasthenia gravis

Yujia Liu[a,b*], Guofang Xia[c*], Huaiying Shi[a*], Simeng Zhu[c], Hailong Li[a,b], Yifan Shi[c], Wanling Ouyang[c], Congfeng Xu [c], and Ailian Du[a,b]

[a]Department of Neurology, Songjiang Hospital Affiliated to Shanghai Jiao Tong University School of Medicine, Shanghai, China; [b]Department of Neurology, Tongren Hospital, Shanghai Jiao Tong University School of Medicine, Shanghai, China; [c]Department of Cardiology, Shanghai Jiao Tong University School of Medicine Affiliated Sixth People's Hospital, Shanghai, China

ABSTRACT

Accelerated CHRN/AChR/nicotinic acetylcholine receptor internalization induced by auto-antibodies impairs neuromuscular junction transmission and contributes to myasthenia gravis (MG), a typical autoimmune disease. Although CHRN internalization is well established in MG pathogenesis, the downstream cellular events, especially those related to autophagy, remain poorly described. Here, we report that RAPSN/rapsyn, an intracellular CHRN-binding protein essential for its clustering, accumulates as aggregates in experimental autoimmune myasthenia gravis (EAMG) mice. In CHRN antibody-treated myotubes, RAPSN dissociates from internalized CHRN and forms aggregates due to exposure of its hydrophobic domains. These aggregates in turn impair the trafficking and membrane incorporation of newly synthesized CHRN, thereby exacerbating CHRN loss. Notably, the accumulation of RAPSN aggregates facilitates formation of HSPA/HSP70-BAG3 complex, which recognizes and transports the aggregates along microtubules to form perinuclear aggresomes for subsequent lysosomal degradation. Accordingly, pharmacological inhibition or knockdown of HSPA-BAG3 complex increases RAPSN aggregation, which participates in enhanced CHRN loss and worsened muscle weakness in EAMG mice. This study identifies HSPA-BAG3 aggrephagy as a protective mechanism that clears RAPSN aggregates to maintain CHRN integrity and suggests a potential therapeutic strategy for MG.

ARTICLE HISTORY
Received 12 December 2025
Revised 17 June 2026
Accepted 18 June 2026

KEYWORDS
Aggregate; autophagy; CHRN; HSPA; myasthenia gravis; RAPSN

Abbreviation: 3-MA: 3-methyladenine; AAV: adeno-associated virus; CASA: chaperone-assisted selective autophagy; CHRN/nicotinic acetylcholine receptor: cholinergic receptor nicotinic; CHRN-ab: CHRN antibodies; CHX: cycloheximide; CMAP: compound muscle action potential; CQ: chloroquine; EAMG: experimental autoimmune myasthenia gravis; ER: endoplasmic reticulum; GAS: gastrocnemius; MAP1LC3A/B: microtubule associated protein 1 light chain 3 alpha/beta; MG: myasthenia gravis; NMJ: neuromuscular junction; Rapa: rapamycin; RAPSN/rapsyn: receptor associated protein of the synapse; SQSTM1: sequestosome 1; TA: tibialis anterior; αBTX-A594: α-bungarotoxin-Alexa-594.

Introduction

Myasthenia gravis (MG) is a classical auto-antibody-mediated autoimmune disorder characterized by muscle weakness ranging from isolated ocular manifestations to life-threatening respiratory compromise [1,2]. Approximately 85% of MG patients are serum-positive for auto-antibodies against the nicotinic acetylcholine receptor (CHRN/AChR), which may lead to complement activation, blocking of acetylcholine binding [2,3], and accelerated internalization and degradation of CHRN [4]. This loss of functional CHRN at endplate is a hallmark of the disease and correlates with the severity of muscle weakness in MG patients [5,6]. Although significant advances have been achieved in understanding the immune-mediated pathogenesis of MG [7], little is known about the intracellular molecular processes elicited by the binding of CHRN antibodies (CHRN-ab).

Physiologically, nerve terminals release the neurotransmitter acetylcholine that stimulates muscle CHRN to trigger postsynaptic action potentials and muscle contraction. The unparalleled efficiency of synaptic transmission is attributable to high-density CHRN clusters at neuromuscular junction (NMJ), approximately reaching 10,000/μm^2 [8]. The formation of CHRN clusters *in vivo* critically depends on the agrin-LRP4-MUSK signaling pathway, which ultimately converges on the activation of RAPSN/rapsyn (receptor associated protein of the synapse), essential for CHRN clustering [9–11]. RAPSN is a 43-kDa intracellular protein originally identified through its co-purification with CHRN from the *Torpedo* electric organ [12]. RAPSN also stabilizes CHRN clusters by anchoring them to the synaptic cytoskeleton, functioning as a key scaffolding molecule

CONTACT Congfeng Xu cxu@shsmu.edu.cn Department of Cardiology, Shanghai Jiao Tong University School of Medicine Affiliated Sixth People's Hospital, No. 600 Yishan Road, Shanghai 200233, China; Ailian Du 734001737@shsmu.edu.cn Department of Neurology, Songjiang Hospital Affiliated to Shanghai Jiao Tong University School of Medicine, No. 746 Zhongshan Middle Road, Shanghai 201600, China
*These authors contributed equally to this work.

Supplemental data for this article can be accessed online at https://doi.org/10.1080/15548627.2026.2693778.

© 2026 The Author(s). Published by Informa UK Limited, trading as Taylor & Francis Group.
This is an Open Access article distributed under the terms of the Creative Commons Attribution-NonCommercial-NoDerivatives License (http://creativecommons.org/licenses/by-nc-nd/4.0/), which permits non-commercial re-use, distribution, and reproduction in any medium, provided the original work is properly cited, and is not altered, transformed, or built upon in any way. The terms on which this article has been published allow the posting of the Accepted Manuscript in a repository by the author(s) or with their consent.

[13]. Beyond these roles at the synapse, RAPSN escorts CHRN during its transport to the sarcolemma following biosynthesis [14,15]. However, excessive RAPSN impairs the docking or fusion of CHRN-rich transport vesicles with the plasma membrane [16]. RAPSN can self-oligomerize via its tetratricopeptide repeat domains [17], raising the question of whether the observed disruption of CHRN clustering is due to the formation of toxic protein aggregates by overexpressed RAPSN. The accumulation of excessive RAPSN in juxtanuclear lysosomes at high density [18,19], together with its observed interaction with HSPA/HSP70 [20], suggests the involvement of an undefined degradation pathway.

Uncontrolled protein aggregation is cytotoxic and is regarded as a hallmark of neurodegenerative diseases such as Alzheimer and Parkinson diseases [21]. When aberrant interactions, mutations, or proteotoxic stresses cause proteins to expose interactive surfaces such as aggregation-prone hydrophobic regions, protein aggregates occur. Sufficient evidence has demonstrated macroautophagy/autophagy as a key cellular process to clear such aggregates [22]. In contrast, the proteasome and chaperone-mediated autophagy (CMA) are only capable of degrading individual protein [22]. Aggrephagy represents the selective form of autophagy targeting protein aggregates, which are typically recognized by cargo receptors such as SQSTM1/p62 (sequestosome 1) and the sequestosome-like receptor NBR1, as well as more recently identified receptors including CCT2 and RNF216/TRIAD3A [23,24], followed by autophagosome formation and consequent lysosomal degradation. As a specific form of aggrephagy, chaperone-assisted selective autophagy (CASA) recognizes substrates through an ATP-regulated transient association with exposed hydrophobic regions by CASA complex, including HSPA and the co-chaperones BAG3 and HSPB8 [25–27]. During the process, BAG3 interacts with dynein, directing the retrograde transport of HSPA substrates to the aggresomes, a perinuclear compartment caged by intermediate filaments and characterized by high autophagic activity, ultimately targeting aggregates to the lysosomes for clearance [26]. Impaired CASA function leads to the accumulation of protein aggregates and compromises muscle integrity [28,29]. Our previous study found that CASA levels may be elevated in the skeletal muscles of experimental autoimmune myasthenia gravis (EAMG) mice [4]. However, the role of CASA in clearing aggregates in MG remains to be elucidated.

In this work, we observed increased RAPSN aggregates in the skeletal muscles of EAMG mice. Following CHRN internalization, RAPSN dissociates from CHRN and self-assembles into aggregates, likely due to its hydrophobic exposure. The accumulation of RAPSN aggregates disrupts the trafficking of newly synthesized CHRN to the plasma membrane. RAPSN aggregates promote the expression of the chaperone HSPA, which is responsible for recognizing and binding RAPSN, and the HSPA-BAG3 complex subsequently transports the aggregates along microtubules to the perinuclear region for aggresome formation and subsequent lysosomal degradation. Inhibition of the HSPA-BAG3 complex in mouse skeletal muscle increases RAPSN accumulation, exacerbates CHRN loss, and worsens muscle weakness. Our study reveals that HSPA-BAG3 aggrephagy pathway protects CHRN from RAPSN aggregate-induced damage, and its dysregulation leads to CHRN destabilization and disease progression in MG.

Results

RAPSN aggregates increase in skeletal muscles of EAMG mice

In skeletal muscles, under certain pathological conditions, misfolded proteins can form insoluble protein aggregates [30]. To examine the role of protein aggregation in MG, we established an EAMG model by immunizing C57BL/6 mice with peptide $\alpha_{146–162}$ (Figure 1A). EAMG mice exhibited typical MG symptoms, including significantly reduced hanging time (Figure 1B), elevated clinical scores (Figure 1C), progressively increased levels of serum CHRN-ab (Figure 1D), and decreased response to repetitive nerve stimulation (Figure 1E, F). Insoluble protein aggregates were isolated as detergent-insoluble pellets (P) following lysis with 1% Triton X-100 (Figure 1G). As the primary pathological target, CHRN showed enhanced degradation in the soluble fraction in EAMG mice (Figure 1H, I), but was not detectable in the insoluble fraction (data not shown). We instead turned our attention to other CHRN-associated proteins. Among them, RAPSN directly anchors CHRN, unlike the transmembrane proteins MUSK and LRP4, which do not interact directly with CHRN. This direct association may render RAPSN particularly vulnerable to disruption of CHRN clusters. Moreover, RAPSN intrinsically oligomerizes under physiological conditions, raising the possibility of pathological aggregation. Interestingly, we observed a substantial 4.6-fold increase in insoluble RAPSN aggregates in EAMG mice, while levels of soluble RAPSN remained unchanged (Figure 1J–L). Immunofluorescence staining displayed a significant increase in punctate RAPSN aggregates adjacent to CHRN clusters labeled by α-bungarotoxin-Alexa-594 (αBTX-A594) within skeletal muscles of EAMG mice (Figure 1M, N). These data suggest the presence of insoluble RAPSN aggregates in skeletal muscles of EAMG mice.

CHRN internalization induces RAPSN aggregation and impairs trafficking of newly synthesized CHRN

Given that RAPSN stability depends on membrane-bound CHRN [31], we supposed that CHRN internalization, a critical pathogenic process in MG, may promote RAPSN aggregation. Using C2C12 myotubes, CHRN clustering was induced with agrin, followed by CHRN-ab treatment to trigger internalization. Consistent with the observations in EAMG mice, soluble CHRN level decreased (Figure 2A, B), while its insoluble fraction remained undetectable (data not shown). Notably, insoluble RAPSN increased under CHRN-ab treatment compared with control IgG (Figure 2A, D), while there was no change in the soluble fraction (Figure 2C). As CHRN-ab is well known to accelerate the internalization of preexisting surface CHRN,

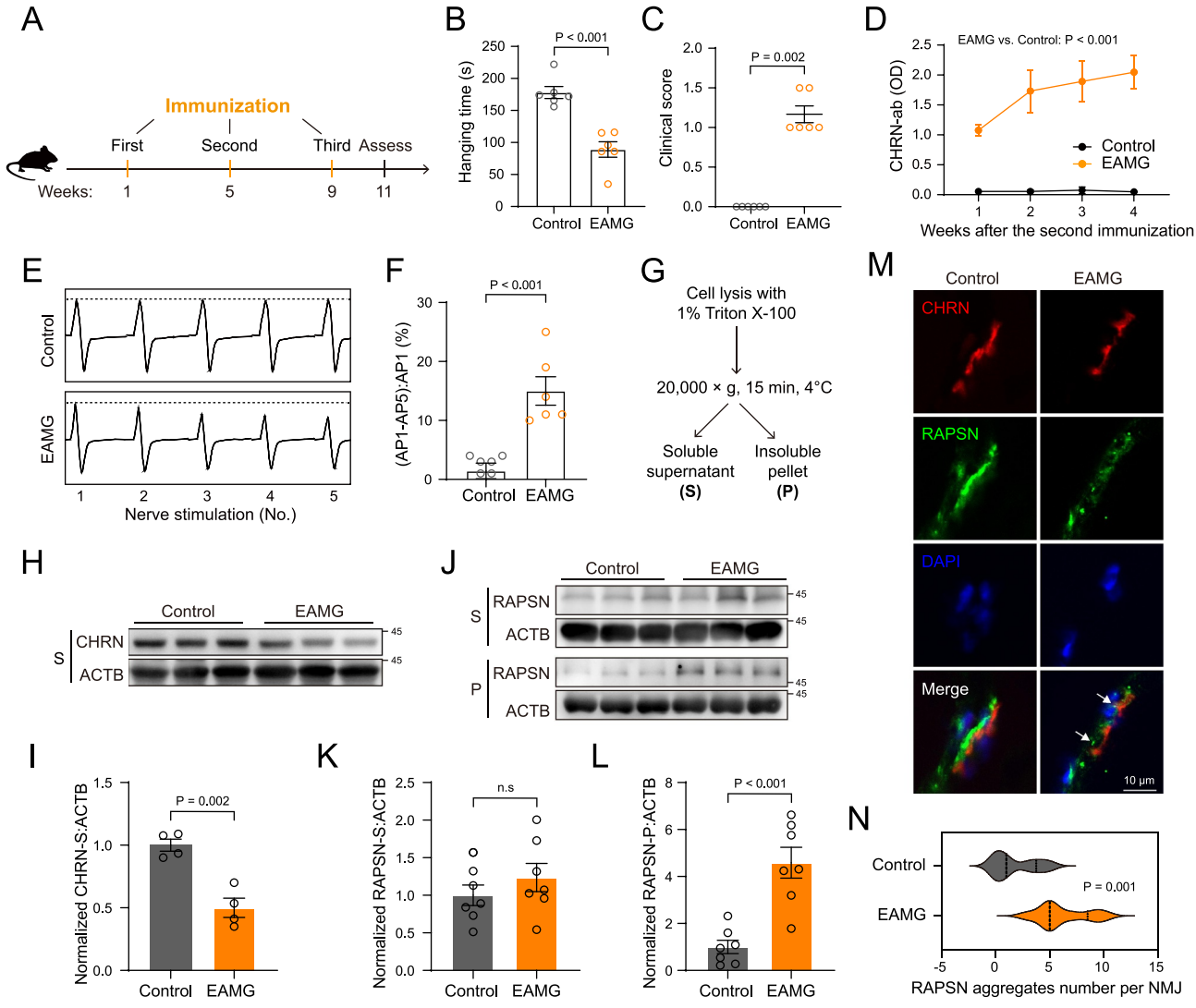

Figure 1. Establishment of EAMG model and increased RAPSN aggregates in EAMG mouse skeletal muscles. (A) Schematic representation of EAMG induction process. Female C57BL/6 mice (6–8 weeks old) were immunized three times with peptide CHRNA/AChR$\alpha_{146–162}$. (B–F) Evaluation of EAMG model, including hanging time assessed by the flip suspension test (B), clinical scores of myasthenic symptoms assessed using the Lennon grading method (0: healthy; 3: severe weakness) (C), serum CHRN-ab titers monitored weekly by ELISA assay (D), representative image of compound muscle action potential (CMAP) under 3-Hz repetitive nerve stimulation recorded from gastrocnemius (GAS) electromyogram (E), and the attenuation rate (%) of the fifth CMAP amplitude (AP5) relative to the first amplitude (AP1) (F) quantified from (E) (n = 6 mice per group). (G) Schematic representation of Triton X-100 extraction of skeletal muscle lysates into soluble supernatant (S) and insoluble pellet (P) fractions. (H and I) Immunoblot (H) and quantification (I) of soluble CHRN in control and EAMG mouse muscles, with ACTB/actin as a loading control (n = 4 mice per group). (J–L) Immunoblot (J) and quantification (K and L) of soluble and insoluble RAPSN in control and EAMG mouse muscles (n = 7 mice per group). (M) Cross sections of GAS muscles from control and EAMG mice stained with αBTX-A594 (CHRN in red), RAPSN antibody (in green), and DAPI (in blue). Arrows point to representative RAPSN aggregates. (N) Quantification of RAPSN aggregate number per NMJ (n = 8 NMJs from 3 mice per group). OD, optical density; No., number; n.s, not significant. Data are presented as means ± SEM. Two-tailed unpaired t test (B, I, K, L, N); Mann-Whitney U test (C and F); two-way ANOVA (D).

we next examined whether the trafficking of newly synthesized CHRN is also altered under these conditions. Since αBTX irreversibly binds CHRN, we employed a two-step labeling strategy to distinguish preexisting and newly synthesized CHRN. Preexisting surface CHRN was first labeled with αBTX-A488 (green) and images were captured prior to CHRN-ab treatment. After induction of CHRN internalization, newly inserted CHRN was subsequently labeled with αBTX-A594 (red) and the images of same myotubes were captured at the end of the experiment (Figure 2E). After 13 h, we observed that the area of surface preexisting CHRN was reduced by approximately 50%, indicating effective internalization. Notably, a similar reduction was observed in the membrane insertion of newly synthesized CHRN within preexisting CHRN clusters (Figure 2F, G). These results indicate that accelerated CHRN internalization leads to RAPSN aggregation and is accompanied by impaired membrane incorporation of newly synthesized CHRN.

RAPSN aggregation driven by dissociation from internalized CHRN impairs CHRN trafficking

As CHRN internalization induced RAPSN aggregate formation, we would like to further explore the interaction between RAPSN and CHRN. To assess changes in CHRN-bound RAPSN during internalization, surface CHRN was labeled in live myotubes with biotin-αBTX, followed by streptavidin

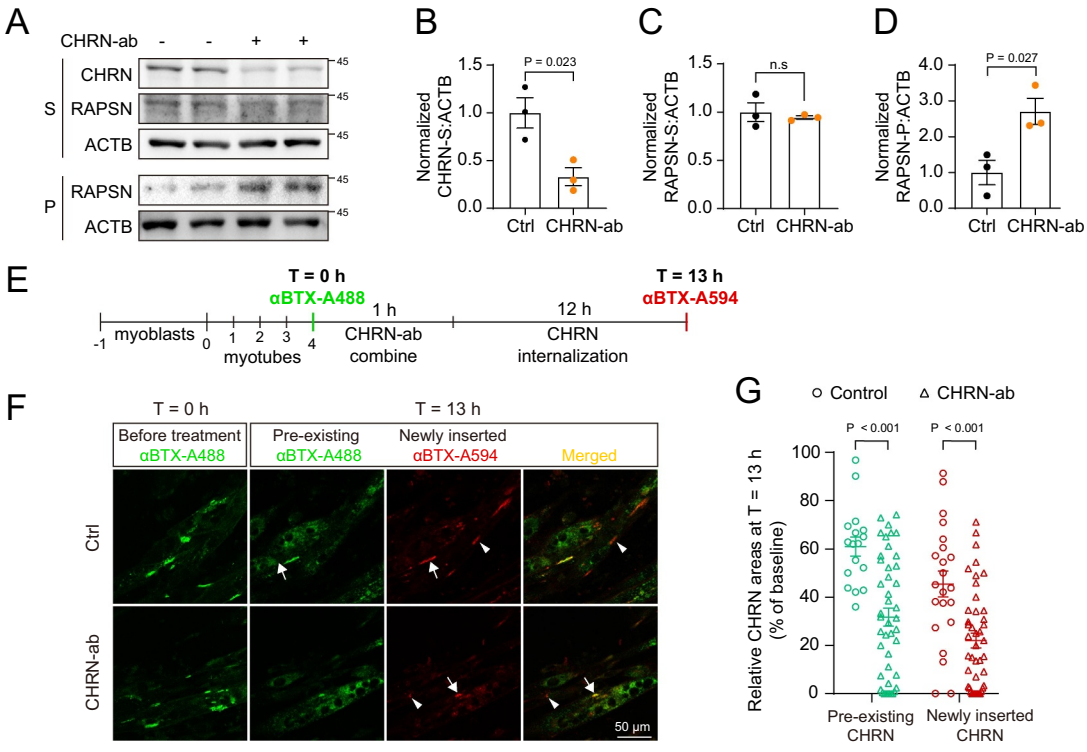

Figure 2. CHRN internalization drives pathological RAPSN aggregation and disrupts CHRN trafficking. (A–D) Immunoblot (A) and quantification (B-D) of soluble CHRN, soluble RAPSN and insoluble RAPSN from three independent experiments. Five-day-old C2C12 myotubes were treated with agrin for 18 h to induce CHRN clustering, followed by pretreatment with CHRN-ab (5 μg/mL) or control mouse IgG (Ctrl) for 1 h at 4°C, followed by CHRN internalization induction for 1 h at 37°C. (E) Schematic representation of the experimental time lapse imaging. (F) Four-day-old C2C12 myotubes were treated with agrin for 18 h, then labeled with αBTX-A488 (green) to mark preexisting CHRN and imaged ($T = 0$ h), followed by pretreatment with CHRN-ab or control mouse IgG and induction of CHRN internalization for a total of 13 h. Then newly inserted surface CHRN was labeled with αBTX-A594 (red) and the same myotubes were imaged again at $T = 13$ h. Insertions of new CHRN clusters are shown in preexisting CHRN clusters (arrow) or in new localizations (arrowhead). (G) Relative area of preexisting CHRN (green) and newly inserted CHRN within preexisting CHRN clusters (red, arrow in F) at $T = 13$ h, shown as the percentage of the same preexisting CHRN area at $T = 0$ h (baseline) (three independent experiments; n = number of CHRN clusters counted, between 17 and 44). n.s, not significant. Data are presented as means ± SEM. Two-tailed unpaired t test (B-D, G).

pull-down of CHRN-interacting proteins. We found that CHRN-bound RAPSN at the plasma membrane was significantly reduced under CHRN-ab treatment compared with control IgG (Figure 3A–C), indicating dissociation of RAPSN from surface CHRN. Live-cell imaging of myotubes transfected with RAPSN-mCherry further confirmed that RAPSN was predominantly localized at the plasma membrane before CHRN-ab treatment, but rapidly dissociated and accumulated as perinuclear aggregates following CHRN internalization (Figure 3D). Internalized CHRN traffics to endosomes [32], and we indeed observed colocalization of CHRN with early (EEA1/RAB5) and late (RAB7) endosome markers, which was enhanced under CHRN-ab treatment (Figure S1A – C). However, no colocalization of RAPSN with these markers was observed (Figure 3E), suggesting that RAPSN dissociates from CHRN rather than co-trafficking with it during internalization. To gain structural insight into this dissociation process, we performed molecular docking analysis (Figure 3F), and identified a hydrophobic patch within RAPSN (10 residues, MET273 to ASP303) that interacted with CHRN (Table S1). To further examine whether exposure of such hydrophobic regions promotes RAPSN aggregation, we heterologously expressed RAPSN in HEK293T cells and observed spontaneous aggregate formation (Figure 3G), which was reduced upon increased CHRN expression (Figure 3H), indicating that association with CHRN limits RAPSN aggregation, likely by shielding hydrophobic interfaces. Given that the exposure of hydrophobic residues to solvent can promote protein aggregation via intermolecular hydrophobic interactions [33,34], we propose that dissociation of RAPSN from CHRN during internalization may expose these buried hydrophobic regions and thereby drive RAPSN self-aggregation.

As RAPSN is essential for the trafficking of newly synthesized CHRN [15], we next sought to determine whether the reduced membrane insertion of newly synthesized CHRN observed in Figure 2G results from accelerated internalization of preexisting CHRN or is directly caused by RAPSN aggregation. To address this, we induced RAPSN aggregation by overexpression and examined CHRN localization (Figure 3I). Compared with vehicle control, RAPSN overexpression significantly reduced membrane CHRN area and increased perinuclear CHRN accumulation (Figure 3J, K), indicating impaired post-translational trafficking of newly synthesized CHRN to the cell surface. Collectively, the data indicate that CHRN internalization induces RAPSN dissociation, leading to the exposure of hydrophobic interfaces that drive its aggregation. RAPSN aggregates in turn impair trafficking of newly synthesized CHRN and limit its membrane incorporation. In addition, RAPSN aggregates undergo a degradation pathway distinct from that of internalized CHRN, which prompted us to further investigate this process.

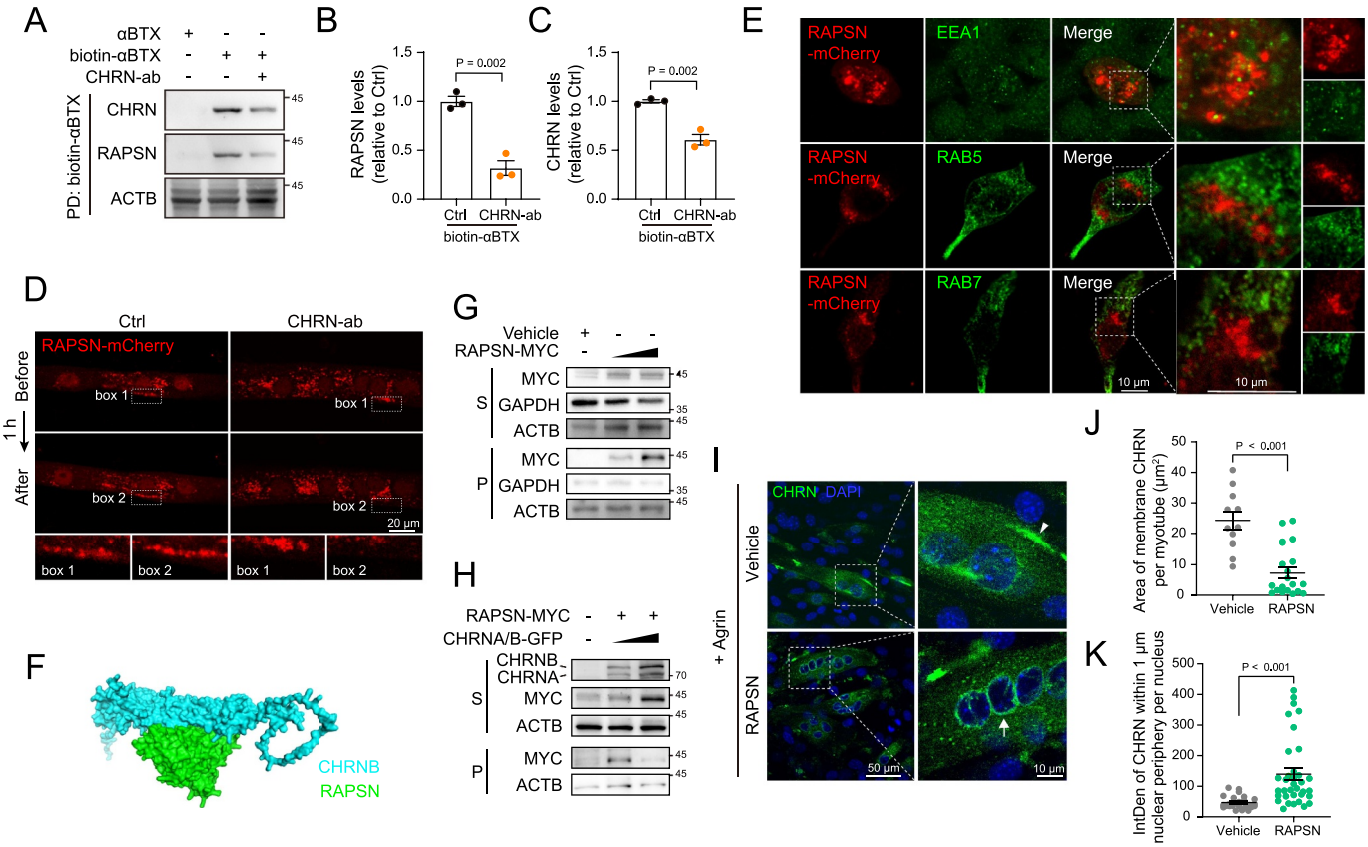

Figure 3. Mechanism of RAPSN aggregate formation and its impact on CHRN trafficking. (A–C) Immunoblot (A) and quantification (B and C) of membrane CHRN and CHRN-bound RAPSN from three independent experiments. Five-day-old C2C12 myotubes were treated with agrin for 18 h, then pretreated with CHRN-ab or control mouse IgG for 1 h at 4°C, followed by induction of CHRN internalization for 1 h at 37°C. Surface CHRN was then labeled with 300 nM biotin-αBTX or αBTX (control) for 2 h at 4°C. CHRN and its bound proteins were subsequently pulled down using streptavidin-coupled dynabeads. (D) Live-cell imaging of RAPSN-mCherry distribution in agrin treated myotubes before (top) and after (bottom) treatment with CHRN-ab or control mouse IgG for 1 h; boxed regions showed membrane-binding RAPSN. (E) Immunofluorescence images of RAPSN-mCherry transfected C2C12 myoblasts stained with the antibody against early endosome marker EEA1 or RAB5, or late endosome marker RAB7. (F) Molecular docking model of RAPSN-CHRNB/AChRβ interaction. (G) Immunoblot of soluble and insoluble RAPSN in CHRN-free HEK293T cells transfected with increasing amounts of RAPSN-MYC. (H) Co-expression analysis in HEK293T cells transfected with RAPSN-MYC and increasing CHRNA/B-GFP. (I) Immunofluorescence images of surface and intracellular CHRN labeled with αBTX-A488 in vehicle or RAPSN-MYC transfected myotubes after agrin treatment. Zoomed images show perinuclear CHRN (arrow) and membrane CHRN cluster (arrowhead). (J) Quantification of membrane CHRN cluster area per myotube from three independent experiments (n = number of cells counted, between 11 and 19). Membrane CHRN area was defined based on αBTX-positive signals localized along lateral edges of the myotubes. (K) Quantification of integrated density (IntDen) of CHRN within 1 μm nuclear periphery per nucleus from three independent experiments (n = number of nucleus counted, between 25 and 35). The perinuclear region was defined as a 1 μm-wide zone surrounding nuclear boundary. PD, pull down. Data are presented as means ± SEM. Two-tailed unpaired t test (B, C, J); Mann-Whitney U test (K).

Autophagy degrades RAPSN aggregates and is upregulated in EAMG

Previous studies have identified the accumulation of overexpressed RAPSN in juxtanuclear lysosomes [18,19], and autophagy serves as a major pathway for degrading protein aggregates. We first investigated the role of lysosomal degradation in RAPSN clearance by treating C2C12 myoblasts with chloroquine (CQ), which effectively inhibited lysosomal function, as confirmed by impaired autophagic flux evidenced by increased levels of SQSTM1 and MAP1LC3A/B (microtubule associated protein 1 light chain 3 alpha/beta)-II (Figure 4A, D, E). CQ not only blocked the degradation of insoluble RAPSN aggregates (Figure 4A, B), but also increased their fluorescence area (Figure 4F, G). In addition, we did observe the functional uptake of RAPSN into lysosomes in HEK293T cells co-transfected with RAPSN-mCherry and LAMP2-EGFP (Figure 4H). To further examine the contribution of autophagy, myoblasts were treated with rapamycin (Rapa), an MTOR inhibitor that activates autophagy, and showed enhanced clearance of RAPSN aggregates and a reduction in fluorescent area (Figure 4A, B, F, G). In contrast, treatment with 3-methyladenine (3-MA), an inhibitor of autophagy initiation, suppressed RAPSN aggregate degradation (Figure S2A, B), supporting a role for autophagy in RAPSN aggregate clearance. Endosomal microautophagy was also reported to regulate the clearance of aggregation-prone proteins [35,36]. However, we observed no colocalization of RAPSN with endosome markers (Figure 3E). In addition, knockdown of LAMP2A, a critical receptor and channel for CMA, did not affect RAPSN aggregate degradation (Figure S2C – F). These data support autophagy, rather than CMA or endosomal microautophagy, as the major pathway for RAPSN aggregate degradation.

However, neither CQ nor Rapa altered soluble RAPSN levels (Figure 4A, C), supporting the selectivity of aggrephagy for RAPSN aggregates. Complementary to above aggrephagy findings, we found that the proteasome inhibitor

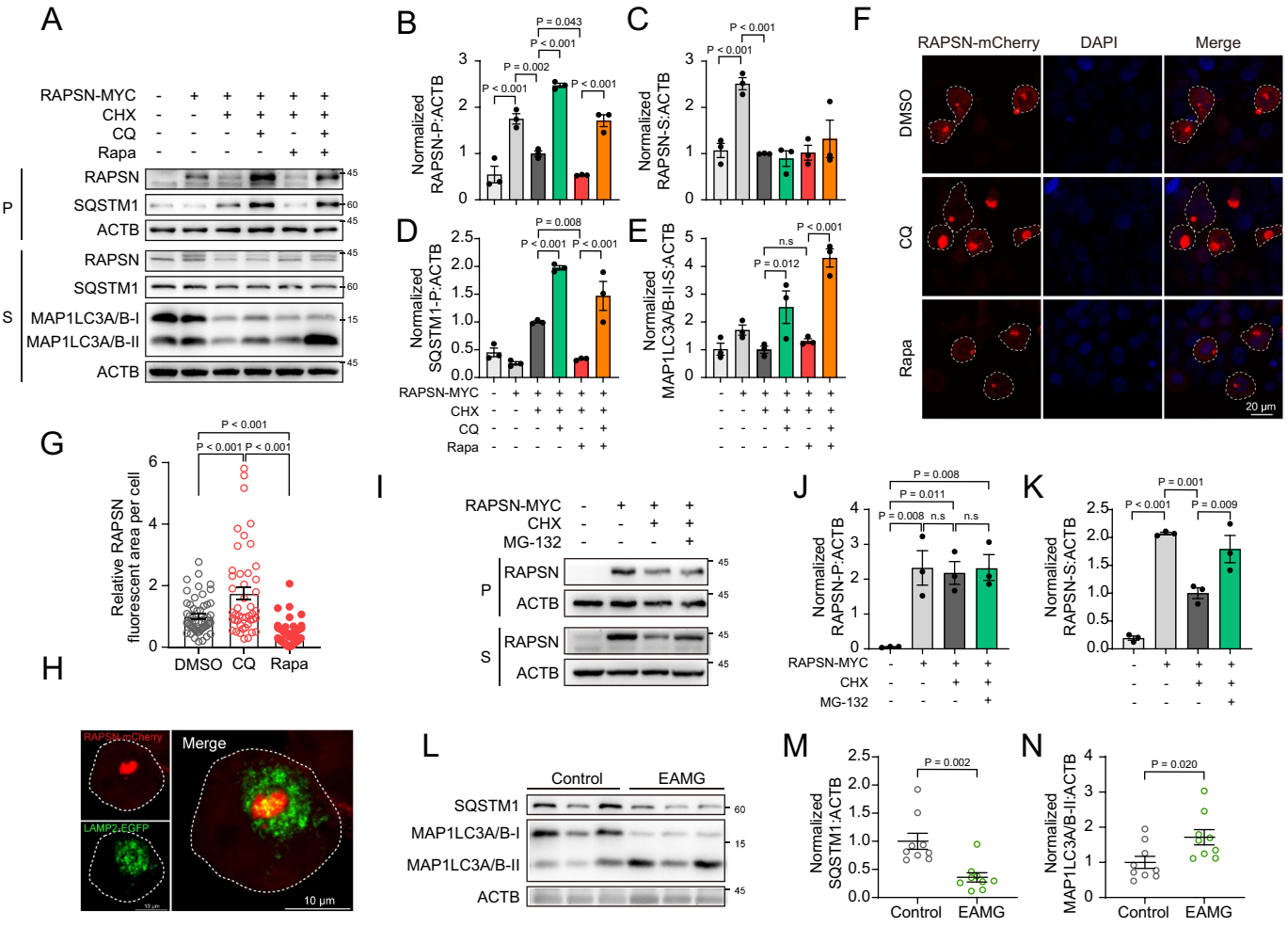

Figure 4. Differential degradation of RAPSN fractions by autophagic-lysosomal and proteasomal systems. (A) Immunoblot analysis of soluble and insoluble RAPSN-MYC degradation and autophagic flux in C2C12 myoblasts under treatment with protein synthesis inhibitor cycloheximide (CHX, 25 μM) ± chloroquine (CQ, 20 μM), rapamycin (Rapa, 200 nM), or both CQ (20 μM) and Rapa (200 nM) for 12 h. (B–E) Quantification of soluble RAPSN and MAP1LC3A/B-II, and insoluble RAPSN and SQSTM1, normalized to CHX-treated RAPSN-MYC transfected myoblasts from three independent experiments. (F) Confocal images of HEK293T cells transfected with RAPSN-mCherry and treated with DMSO, CQ or Rapa. (G) Quantification of the fluorescent area of RAPSN-mCherry aggregates per cell, normalized to the DMSO group (three independent experiments; *n* = number of cells counted, between 45 and 88). (H) Representative colocalization image of RAPSN-mCherry and LAMP2-EGFP in HEK293T cells. (I–K) Immunoblot (I) and quantification (J and K) of soluble and insoluble RAPSN-MYC degradation in C2C12 myoblasts under treatment with CHX (25 μM) ± MG-132 (2 μM) for 12 h from three independent experiments. (L–N) Immunoblot (L) and quantification (M and N) of SQSTM1 and MAP1LC3A/B-I/II in EAMG and control mouse muscles (*n* = 9 mice per group). Data are presented as means ± SEM. Two-tailed unpaired *t* test (N); Mann-Whitney U test (M); one-way ANOVA (B-E, G, J, K).

MG-132 specifically prevented the degradation of soluble RAPSN without affecting insoluble RAPSN (Figure 4I–K), revealing the proteasome-selective degradation of soluble RAPSN. Notably, we observed enhanced autophagy flux evidenced by SQSTM1 reduction and MAP1LC3A/B-II elevation in skeletal muscles of EAMG mice compared with controls (Figure 4L–N). Collectively, these findings suggest that RAPSN aggregates are selectively targeted for degradation via autophagy, a process that was enhanced in EAMG mice.

HSPA-BAG3 complex is upregulated and mediates RAPSN aggregate degradation in EAMG

As mentioned above, the RAPSN aggregates were selectively degraded by aggrephagy. The HSPA-BAG3-mediated CASA pathway is well established to facilitate the clearance of pathological protein aggregates [21], and our previous research also suggested its potential involvement in the pathogenesis of MG [4]. We therefore investigated whether the HSPA-BAG3 complex regulates RAPSN aggregates in EAMG. In skeletal muscles of EAMG mice, we observed significant upregulation of both HSPA and its co-chaperone BAG3 at the protein level (Figure 5A–C). Transcriptional analysis further confirmed the specific increase in *Hspa1a* mRNA, with no changes in its homolog *Hspa8* or the established soluble RAPSN regulator *Hsp90ab1* (Figure S3A – C). Immunofluorescence staining also displayed increased fluorescence signal areas for HSPA and BAG3 (Figure S3E – G), together with enhanced colocalization between RAPSN and HSPA in EAMG mice (Figure 5D–F), suggesting a potential interaction between RAPSN aggregates and HSPA. To determine whether RAPSN aggregates

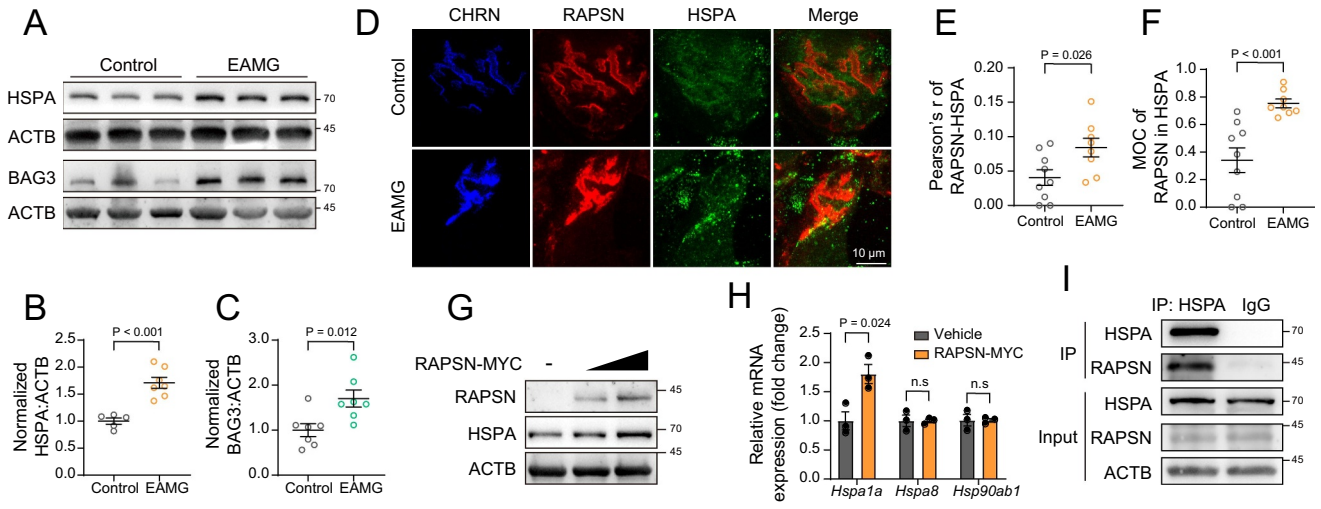

Figure 5. HSPA-BAG3-mediated CASA is upregulated in response to RAPSN aggregates. (A–C) Immunoblot (A) and quantification (B and C) of HSPA and BAG3 in EAMG and control mouse muscles (n = number of mice per group, between 5 and 7). (D) Longitudinal sections of GAS muscles from EAMG and control mice stained for CHRN (in blue), RAPSN (in red), and HSPA (in green). (E and F) Colocalization analysis between RAPSN and HSPA using Pearson's correlation coefficient (r) (E) and Mander's overlap coefficient (MOC) (F) (n = number of NMJs counted from 3 mice per group, between 8 and 9). (G) Immunoblot of HSPA protein in C2C12 myoblasts transfected with vehicle or increasing amounts of RAPSN-MYC. (H) mRNA levels of *Hspa1a, Hspa8*, and *Hsp90ab1* in C2C12 myoblasts transfected with vehicle or RAPSN-MYC from three independent experiments. (I) Endogenous co-immunoprecipitation of HSPA with RAPSN in myotubes. Lysates were immunoprecipitated with anti-HSPA antibody or IgG control. Data are presented as means ± SEM. Two-tailed unpaired t test (B, C, E, F, H).

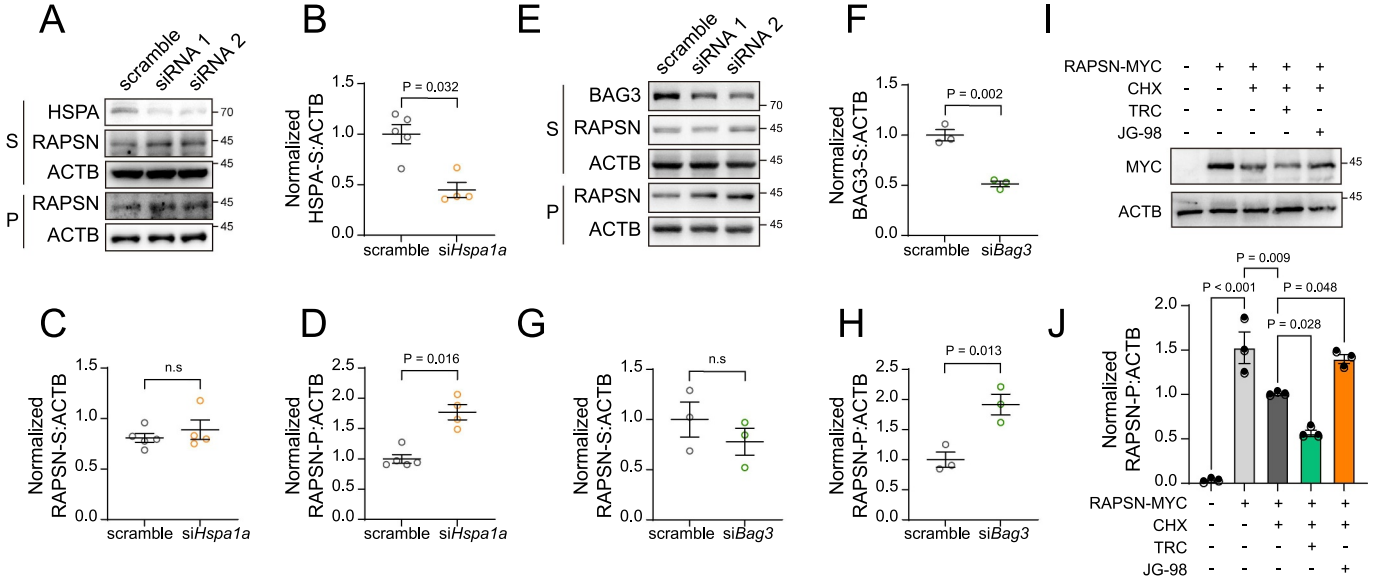

Figure 6. The CASA complex regulates the degradation of RAPSN aggregates. (A–H) Immunoblot analysis of soluble and insoluble RAPSN levels in C2C12 myotubes transfected with scramble control siRNA or siRNA targeting *Hspa1a* (A) or *Bag3* (E). Quantification of HSPA (B) and BAG3 (F) protein levels, and corresponding soluble (C and G) and insoluble (D and H) RAPSN levels. Data are from three independent experiments. (I and J) Immunoblot (I) and quantification (J) of insoluble RAPSN-MYC in C2C12 myoblasts treated with CHX (25 μM) ± TRC (10 μM) or JG-98 (1 μM) for 12 h from three independent experiments. Data are presented as means ± SEM. Two-tailed unpaired t test (C, F, G, H); Mann-Whitney U test (B and D); one-way ANOVA (J).

themselves trigger HSPA complex recruitment, we overexpressed RAPSN in C2C12 myoblasts and observed a specific upregulation of HSPA expression (Figure 5G, H), consistent with the specificity observed in Figure S3A – C. Co-immunoprecipitation assays confirmed an interaction between RAPSN and HSPA (Figure 5I), suggesting that HSPA acts as a chaperone capable of recognizing and binding RAPSN. Functionally, knockdown of HSPA or BAG3 via siRNA significantly increased RAPSN aggregate accumulation to similar levels, without affecting soluble RAPSN (Figure 6A–H). In addition, TRC051384 (TRC), an HSPA transcriptional inducer (Figure S4A, B) [37], accelerated the degradation of RAPSN aggregates. In contrast, the allosteric inhibitor JG-98, which can disrupt the HSPA-BAG3 interaction (Figure S4C) [38], suppressed this degradation process (Figure 6I, J). Altogether, these results demonstrate that RAPSN aggregates are associated with HSPA expression and recruitment, thereby

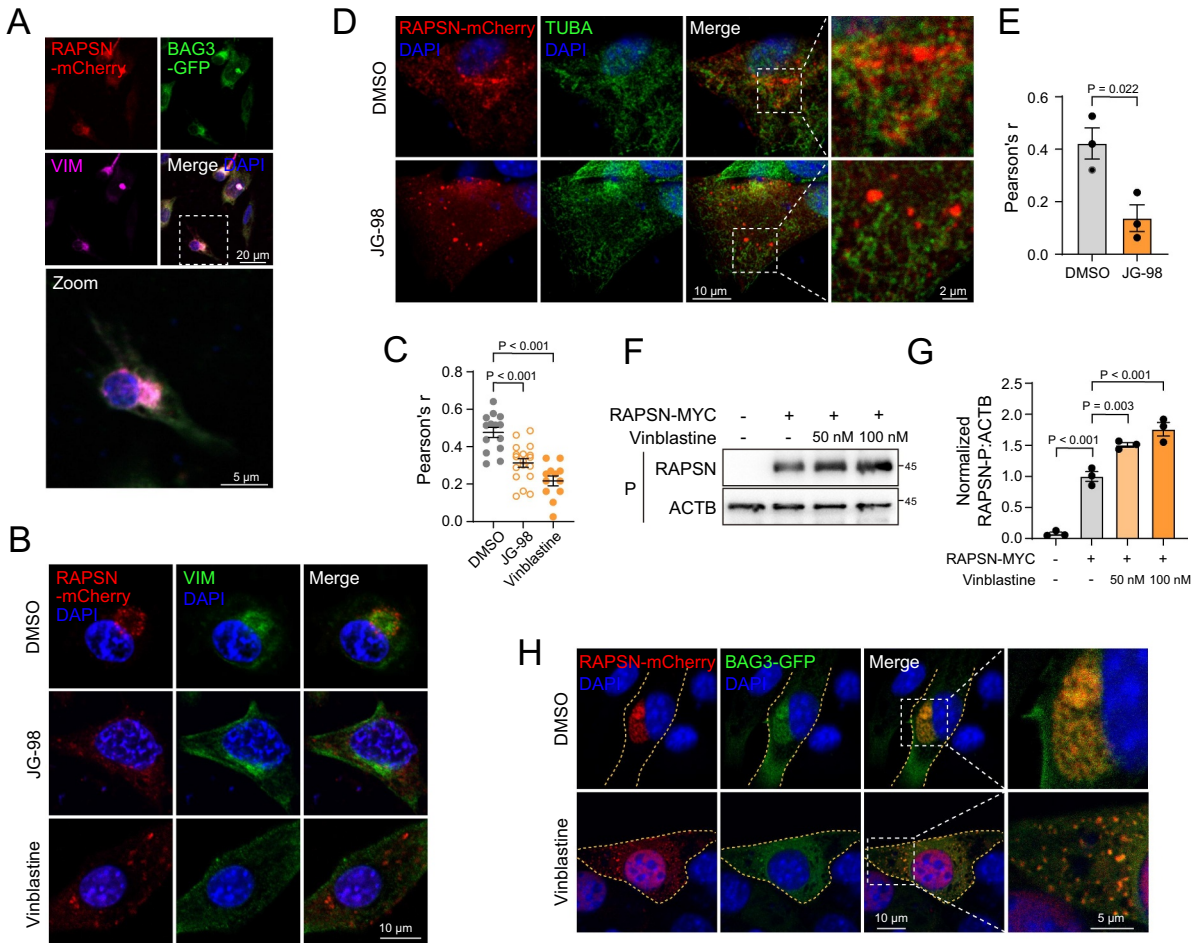

Figure 7. The CASA complex facilitates RAPSN aggregate transport along microtubules and aggresome formation. (A) Immunofluorescence of C2C12 myoblasts co-expressing RAPSN-mCherry and BAG3-GFP for 48 h. Aggresomes were labeled with an anti-VIM antibody. (B and C) Immunofluorescence images (B) and colocalization analysis (C) of RAPSN and VIM in C2C12 myoblasts transfected with RAPSN-mCherry for 48 h and treated with JG-98 for the final 12 h or vinblastine for the final 24 h. The graph showed the Pearson's correlation coefficient (r) between RAPSN and VIM (three independent experiments; *n* = number of cells counted, between 12 and 18). (D and E) Immunofluorescence images (D) and colocalization analysis (E) of RAPSN and TUBA in C2C12 myoblasts transfected with RAPSN-mCherry for 24 h and treated with JG-98 or DMSO for the final 12 h. The graph showed the Pearson's correlation coefficient between RAPSN and TUBA. (F and G) Immunoblot (F) and quantification (G) of RAPSN-MYC aggregate levels in C2C12 myoblasts treated with vinblastine (50 nM or 100 nM) for 24 h from three independent experiments. (H) Immunofluorescence images of RAPSN-mCherry and BAG3-GFP in C2C12 myoblasts transfected for 48 h and treated with vinblastine (50 nM) or DMSO for the final 24 h. Data are presented as means ± SEM. Two-tailed unpaired *t* test (E); one-way ANOVA (C and G).

facilitating subsequent clearance of RAPSN aggregates via the CASA pathway in EAMG.

HSPA-BAG3 complex recruits RAPSN aggregates onto microtubules for transport to perinuclear aggresomes

Aggresomes function as critical intermediates for the selective degradation of protein aggregates via aggrephagy and are characterized by the collapse of the intermediate filament VIM/vimentin [22,39]. Our immunofluorescence analysis showed clear perinuclear colocalization of RAPSN with both VIM and BAG3 at 48 h post-transfection (Figure 7A), suggesting that BAG3-positive RAPSN aggregates could be sequestered into aggresomes. Consistently, treatment with the HSPA-BAG3 complex inhibitor JG-98 markedly reduced RAPSN-VIM colocalization (Figure 7B, C), indicating involvement of the HSPA-BAG3 complex in RAPSN aggresome formation. Prior to aggresome formation, protein aggregates have been shown to undergo microtubule-dependent transport mediated by the HSPA-BAG3 complex [40]. We next determined whether this complex mediates the association of RAPSN aggregates with microtubules. At 24 h post-transfection, before aggresome formation, we found that inhibitor JG-98 significantly reduced the Pearson's correlation coefficient (r) between RAPSN and TUBA/α-tubulin (Figure 7D, E). Consistently, co-immunoprecipitation assay showed that JG-98 decreased the association between RAPSN-MYC and TUBA, indicating the role of HSPA-BAG3 complex in substrate-microtubule binding (Figure S4D). We further disrupted microtubule integrity using the depolymerizing agent vinblastine, and the results showed that vinblastine inhibited the degradation of RAPSN aggregates (Figure 7F, G). Moreover, vinblastine completely suppressed the perinuclear accumulation of BAG3- and aggresome-positive RAPSN structures (Figure 7B, H). Instead, multiple BAG3-positive RAPSN aggregates were dispersed throughout the cytoplasm without forming aggresomes (Figure 7H), highlighting an essential role for microtubules in RAPSN aggregate transport and aggresome formation. Collectively, these

findings demonstrate that HSPA-BAG3 complex serves a critical role in recruiting RAPSN aggregates to microtubules, thereby enabling their transport to perinuclear aggresomes for clearance.

HSPA-BAG3-mediated aggrephagy protects against the disruption of CHRN cluster integrity and mitigates the progression of muscle weakness in EAMG

Given the critical role of HSPA-BAG3-mediated aggrephagy degradation of RAPSN aggregates, together with our finding that these aggregates impair CHRN trafficking, we further investigated whether this degradative pathway is functionally critical for preserving CHRN cluster integrity in myotubes and *in vivo*. Our results showed that BAG3 knockdown significantly reduced the area of both laminin-induced pretzel-like CHRN clusters formed at the basal interface and agrin-induced linear CHRN clusters distributed along the lateral membrane of myotubes (Figure 8A–C). As expected, inhibition of HSPA-BAG3 with JG-98 or lysosomal function with CQ also decreased laminin-induced CHRN cluster areas, whereas autophagy induction with Rapa increased them (Figure S5A, B). Intraperitoneal injection of JG-98 during the final two weeks of immunization led to increased accumulation of RAPSN aggregates in tibialis anterior (TA) muscles of EAMG mice, while soluble RAPSN levels remained unchanged (Figure 8D–G). Notably, this *in vivo* treatment significantly diminished the compactness of CHRN clusters in TA muscles (Figure 8H–J), and increased the proportion of abnormal CHRN morphologies characterized by plaque and ring shapes within diaphragm in EAMG +JG-98 group compared with EAMG group (Figure S5C, D). These structural alterations were accompanied by more severe myasthenic symptoms in the EAMG+JG-98 group (Figure 8K, L), indicating aggravated neuromuscular transmission failure. As shown in Figures 2F, G and 3I–K, our data demonstrate that RAPSN aggregation impairs CHRN intracellular trafficking. Thus, we propose that the accumulation of RAPSN aggregates in EAMG+JG-98 group participates in CHRN cluster impairments and the exacerbation of myasthenic phenotypes. We note that this effect is likely mediated in part by RAPSN aggregation, because other HSPA-BAG3 client proteins affected by JG-98 may also be involved. To further evaluate this, we examined the well-established CASA substrate FLNC and found no significant changes in its levels (Figure S6A, B). Consistently, the FLNC-associated Z-disc structure, marked by ACTN/α-actinin, remained intact across these three groups, indicating no detectable sarcomeric disruption (Figure S6C). These findings suggest that CASA inhibition preferentially affects substrates with increased aggregation burden rather than those maintained at basal turnover levels.

To further exclude potential off-target effects of JG-98, we knocked down HSPA via efficient adeno-associated virus (AAV) injection in both GAS muscles of EAMG mice (Figure 8M, N). Compared with control AAV-injected EAMG mice, HSPA knockdown further increased RAPSN aggregate accumulation (Figure 8O–Q), exacerbated the reduction in CHRN cluster compactness (Figure 8R, S), and decreased both hanging time and muscle strength (Figure 8T, U). Notably, serum CHRN-ab titers remained unchanged between HSPA knockdown and control AAV groups, suggesting that the observed muscle weakness was not attributable to upstream humoral immunity alterations (Figure S6D). Together, our findings demonstrate that HSPA-BAG3-mediated aggrephagy serves as a protective mechanism in MG by recognizing and binding the increased RAPSN aggregates, facilitating their transport along microtubules, and ultimately promoting their lysosomal degradation (Figure 9). Inhibition of HSPA-BAG3 complex is associated with the accumulation of RAPSN aggregates, and these aggregates participate in impairing CHRN cluster integrity and worsening myasthenic phenotypes in MG (Figure 9).

Discussion

In our study, we demonstrate that antibody-induced CHRN internalization leads to the dissociation of its essential scaffolding protein, RAPSN, which subsequently assembles into insoluble aggregates. Excessive RAPSN aggregates impair the trafficking and membrane incorporation of newly synthesized CHRN, thereby impairing synaptic transmission at the NMJ in MG. Here, our observations unveil a previously underappreciated downstream cellular event in MG pathogenesis, highlighting that auto-antibodies exert effects beyond mere loss of CHRN to disrupt the proteostability of the key synaptic organizer RAPSN. Importantly, HSPA-BAG3 complex-mediated aggrephagy participates in the recognition, transport, and degradation of RAPSN aggregates, which is upregulated and plays a protective role in MG.

As a critical linker between neural signals and muscle contraction, it is understandable that CHRN stability and synaptic localization are dynamically regulated in multiple processes, including post-biosynthetic trafficking, clustering, maintenance, and controlled degradation. RAPSN plays a central role in these processes, as evidenced by RAPSN mutations causing CHRN cluster deficiencies in congenital myasthenic syndromes [41]. Following the activation of agrin-LRP4-MUSK cascade, RAPSN undergoes tyrosine phosphorylation and possesses E3 ligase activity [10,11]. This activity leads to neddylation of CHRN and stimulates CHRN clustering. Beyond signaling, RAPSN also serves as a scaffolding molecule through direct CHRN binding via coiled-coil domains and self-oligomerization through its tetratricopeptide repeat domains, further interacting with cytoskeletal proteins like dystroglycan to stabilize CHRN clusters and thereby support muscle contraction [13].

In the absence of RAPSN, the synthesis of CHRN is thwarted, and the limited CHRN trafficking to the postsynaptic membrane is also unstable, prone to internalization and degradation, leading to progressive CHRN depletion at endplates. This is consistent with the observation that RAPSN co-transfection reduces CHRN-ab induced CHRN loss [42], while RAPSN silencing in adult rat muscles decreases CHRN levels by 36% within two weeks [43]. Our data provide cellular evidence that CHRN internalization causes the reduction of membrane-associated RAPSN, a phenomenon similar to the

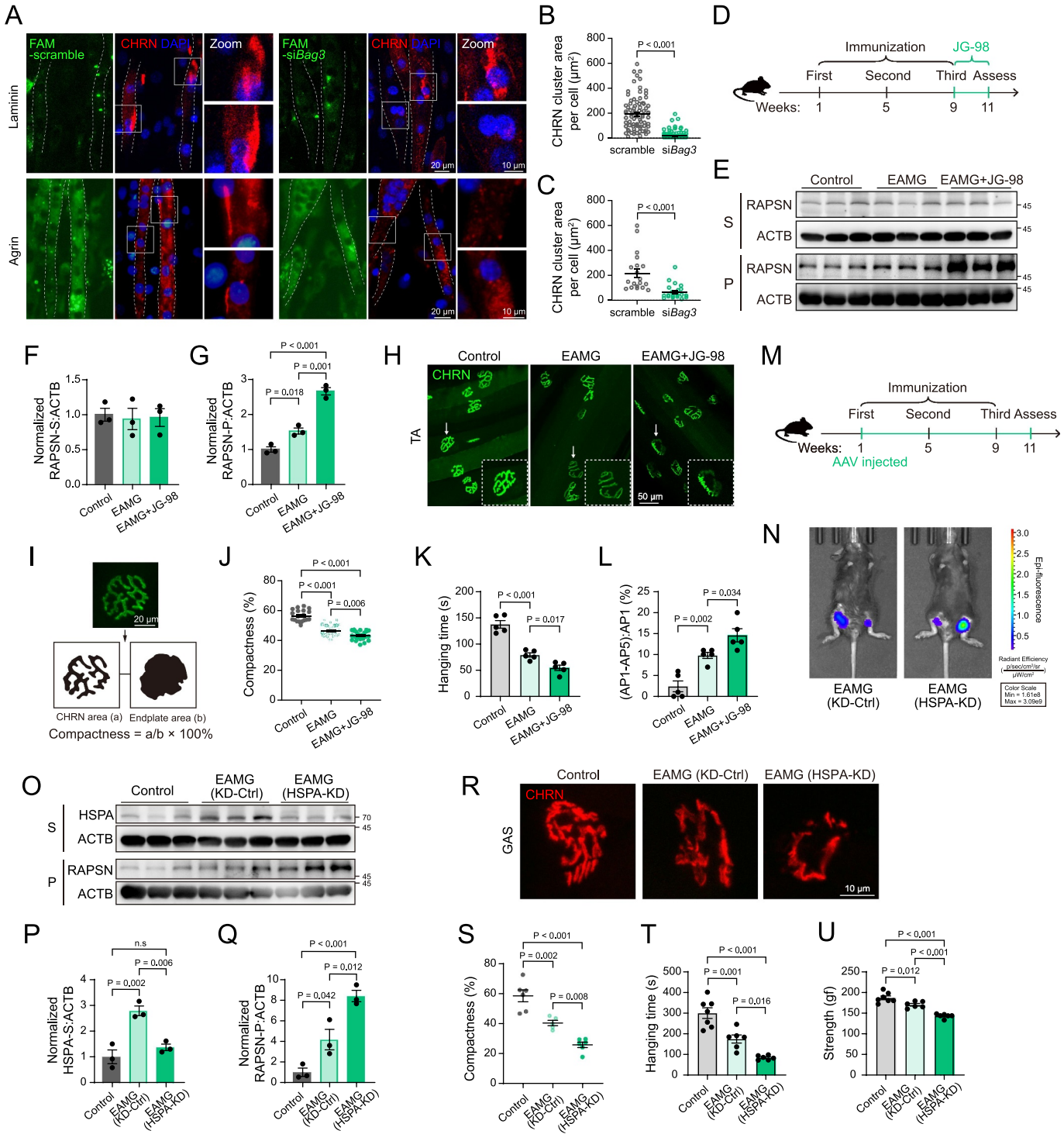

Figure 8. HSPA-BAG3 complex inhibition disrupts CHRN cluster integrity and aggravates muscle weakness in EAMG mice. (A) CHRN clusters on FAM-scramble- and FAM-si*Bag3*-transfected C2C12 myotubes labeled with αBTX-A594 after laminin or agrin treatment to induce the formation of CHRN clusters. (B and C) Quantification of CHRN cluster area from three independent experiments with laminin (B) or agrin (C) (three independent experiments; *n* = number of myotubes counted, between 77 and 80 in B, 19 and 20 in C). (D) Schematic representation of the JG-98 (1 mg/kg) intraperitoneal injection during EAMG induction, administered every other day for two weeks starting from the third immunization. (E-G) Immunoblot (E) and quantification (F and G) of soluble and insoluble RAPSN in control, EAMG, and EAMG +JG-98 mouse muscles (*n* = 3 mice per group). (H) CHRN clusters in TA muscle bundles labeled with αBTX-A488. Arrows indicated representative clusters, with zoomed views shown. (I) Schematic of the method for quantifying CHRN cluster compactness. (J) Quantitative analysis of CHRN cluster compactness in TA muscle bundles from 4 control, 6 EAMG, and 6 EAMG+JG-98 mice (*n* = number of NMJs counted, between 19 and 24). (K and L) Hanging time (K) and CMAP attenuation rate in GAS electromyogram (L) (*n* = 5 mice per group). (M) Schematic representation of AAV9-Ctrl-EGFP (EAMG (KD-Ctrl) group) or AAV9-*Hspa1a* shRNA-EGFP (EAMG (HSPA-KD) group) injection into GAS muscles of EAMG mice at the first immunization. (N) Small-animal live imaging of EAMG mice 30 days after AAV injection as shown in (M). (O–Q) Immunoblot (O) and quantification (P and Q) of soluble HSPA and insoluble RAPSN in control, EAMG (KD-Ctrl), and EAMG (HSPA-KD) groups (*n* = 3 mice per group). (R and S) Longitudinal sections of GAS muscles with CHRN clusters labeled by αBTX-A594 (R) and compactness quantitative analysis of CHRN clusters (S) from 3 mice per group (*n* = number of NMJs counted, between 5 and 6). (T and U) Quantitative analysis of hanging time (T) and whole-limb strength measured by dynamometer (U) (*n* = number of mice counted, between 6 and 7). KD, knockdown. n.s, not significant. Data are presented as means ± SEM. Mann-Whitney U test (B and C); one-way ANOVA (F, G, J-L, P, Q, S-U).

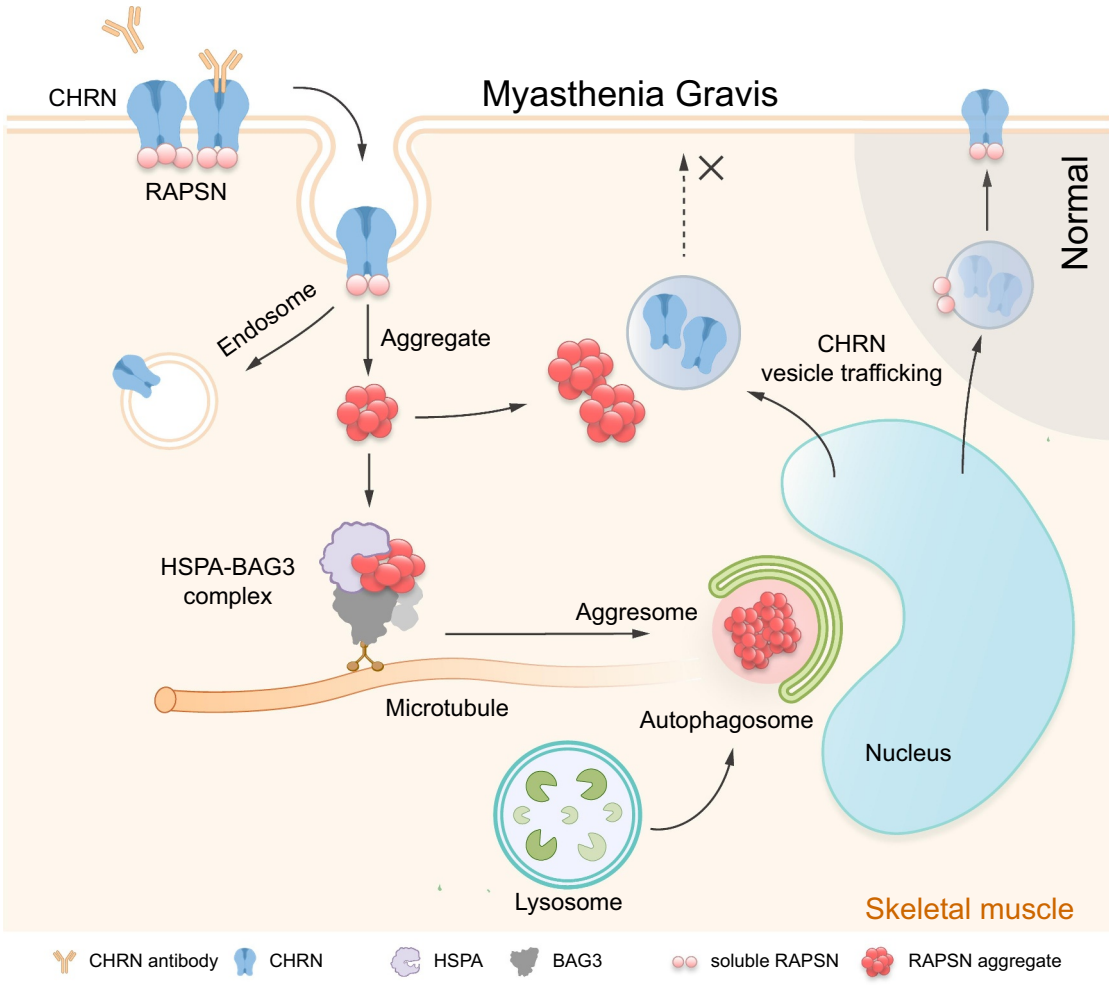

Figure 9. Schematic model of the RAPSN-linked pathogenic cascade and degradation pathway in MG. Key steps are as follows: (1) CHRN-ab binding induces CHRN internalization and RAPSN dissociation; (2) dissociated RAPSN undergoes aggregation following hydrophobic exposure, disrupting CHRN vesicular trafficking and clustering; (3) RAPSN aggregates are recognized by the HSPA-BAG3 complex; (4) the HSPA-BAG3 complex facilitates microtubule-dependent retrograde transport of RAPSN aggregates to form perinuclear aggresomes; (5) RAPSN-positive aggresomes are degraded via lysosomes.

RAPSN dispersion caused by laser-induced CHRN cluster disruption in myotubes [31]. We therefore propose that in MG, the pathological detachment of RAPSN from the postsynaptic membrane results in CHRN impairment by destabilizing remaining CHRN clusters and promoting their degradation.

Beyond its role in membrane clustering, CHRN undergoes vesicle transport escorted by RAPSN to the postsynaptic membrane after biosynthesis and glycosylation in the endoplasmic reticulum (ER) and Golgi apparatus [14,15]. Protein aggregates exhibit inherent toxicity, and larger microscopically detectable aggregates can trap other cellular proteins, leading to secondary loss of function [44]. Our data indicate that RAPSN aggregates impede this vesicular transport process, either by trapping newly synthesized CHRN or directly disrupting receptor turnover, impairing normal intracellular trafficking [45]. The mechanism by which RAPSN aggregates interfere with CHRN vesicular transport remains elusive and requires further investigation. Besides, unlike many structural scaffold proteins, RAPSN exhibits a remarkably high turnover rate in muscle cells, 4–6 times faster than that of CHRN [46], highlighting the necessity of its continuous replenishment for CHRN regulation. RAPSN aggregation also slows this replenishment and leads to functional RAPSN deficiency, without compensatory transcriptional upregulation in MG (Figure S3D).

RAPSN aggregation represents a dynamic process, evolving from nanometer-scale toxic aggregates recognized by HSPA to micrometer-scale aggresomes representing organized sequestration into macromolecular assemblies conducive to lysosomal degradation [44]. In this study, we also confirm proteasomal degradation of soluble RAPSN, consistent with previous research establishing that Hsp90β maintains RAPSN homeostasis by facilitating its turnover in the soluble fraction, which can be inhibited by proteasome inhibitor [20]. In contrast, insoluble RAPSN neither activates Hsp90β nor undergoes proteasomal degradation. This functional partitioning aligns with the established chaperone “triage” model, where Hsp90 generally acts as a stabilizer that protects proteins from unfolding and aggregation, while HSPA directs substrates for degradation when aggregation becomes irreversible [47]. In EAMG skeletal muscles, significant HSPA upregulation represents an adaptive response to proteostatic stress from RAPSN aggregate accumulation, which likely results from insufficient

activation of the Hsp90β-mediated proteasomal degradation pathway (Figure S3A – C). Moreover, HSPA recognizes highly hydrophobic stretches [48], offering a mechanistic basis for how HSPA identifies and binds to hydrophobic domains exposed upon the dissociation of RAPSN from CHRN. Despite the upregulation of HSPA in EAMG mice, the increased RAPSN aggregates suggest that the burden of aggregation exceeds the compensatory capacity of HSPA-mediated aggrephagy.

A remaining unresolved question is whether the clearance of RAPSN aggregates via aggrephagy is ubiquitin-dependent, as ubiquitination is not necessarily for CASA substrates [40], while protein aggregates are commonly recognized and tagged by specific E3 ubiquitin ligases, such as CHIP, UBR1, and SAN1, which facilitate their clearance [49,50]. In addition to CASA, future studies should also explore whether the canonical SQSTM1-NBR1-dependent aggrephagy pathway or the novel aggrephagy receptor CCT2 and TRIAD3A participate in recognizing and clearing aberrant RAPSN aggregates, especially if they become heavily ubiquitinated. Elucidating the role of ubiquitination is essential for understanding the molecular mechanisms of proteostatic dysregulation in MG. To further explore the role of the HSPA-BAG3 complex in EAMG mice, we chose JG-98 as an inhibitor because it selectively disrupts the HSPA-BAG3 interaction without broadly inhibiting HSPA ATPase activity or globally suppressing HSPA functions [51]. In the EAMG+JG-98 group, we observed no significant alterations in the established CASA substrate FLNC and Z-disc integrity in skeletal muscles. Nevertheless, we cannot fully exclude the possibility that other CASA substrates may contribute to CHRN fragmentation and aggravated myasthenic phenotype. Clinical evidence of ER stress upregulation in MG patient muscles [52], together with our previous finding that ER stress promotes CHRN degradation [53], points to significant proteostatic disruption. The accumulation of RAPSN aggregates may exacerbate ER stress, thereby inducing the unfolded protein response and contributing to postsynaptic proteostatic failure. Consistent with this, HSPA is known to be preferentially induced under stress conditions to exert protective functions [54], and its upregulation together with enhanced autophagy in EAMG skeletal muscle suggests the presence of additional pathogenic protein aggregates. Therefore, while our data support RAPSN aggregation as a mechanism, the potential involvement of broader proteostatic imbalance and aberrant protein aggregation in MG pathogenesis requires further research.

Altogether, our study extends the well-established mechanisms of antibody-induced complement activation and CHRN internalization in MG by revealing that CHRN-ab binding additionally disrupts the crucial interaction between CHRN and its scaffolding protein RAPSN. Once dissociated, RAPSN becomes prone to aggregation due to the exposure of its hydrophobic patch. RAPSN aggregate formation directly impairs CHRN vesicular trafficking and clustering, as well as the essential scaffolding function of RAPSN. The increased burden of RAPSN aggregates promotes HSPA expression, and the HSPA-BAG3 complex subsequently facilitates recognition and retrograde microtubule-dependent transport of these aggregates to the perinuclear region, where they are organized into aggresomes and ultimately degraded by lysosomes, a process collectively referred to as HSPA-BAG3-mediated aggrephagy. Thus, our study outlines a cascade from RAPSN dissociation and aggregation to impaired CHRN trafficking, outlining a novel pathogenic mechanism in MG (Figure 9). Potentially, targeting the RAPSN aggregate degradation pathway may represent a promising therapeutic strategy to restore CHRN integrity in MG.

Materials and methods

Mice

Female C57BL/6 mice (6–8 weeks old) were purchased from Beijing Vital River Laboratory Animal Technology Co., Ltd., and were kept under specific pathogen-free conditions in the Laboratory Animal Center of Shanghai Jiao Tong University (Shanghai, China). As MG has a higher prevalence in women, female mice were selected for this animal model. All mouse experiments were approved by the Animal Welfare & Ethics Committee of the Shanghai Jiao Tong University (A2024396).

Establishment of EAMG model

Mice were housed under specific pathogen-free conditions with a 12-h light/dark cycle. One week after adaptive feeding and observation, the mice were randomly divided into solvent control and EAMG groups. 50 μg of peptide CHRNA/AChRα$_{146–162}$ emulsified in Complete Freund's Adjuvant (Sigma-Aldrich, F5881; CFA) was subcutaneously injected at four sites (200 μL/mouse) of each EAMG mouse referenced as described by Tuzun et al [55]. Control mice received CFA emulsion without peptide. Injection sites were two hind foot-pads and over the scapula for the first immunization, and scapula and thighs for subsequent immunizations. Booster immunizations were administered at 4-week intervals using the same antigen emulsified in Incomplete Freund's Adjuvant (Sigma-Aldrich, F5506; IFA). Immunizations were performed according to the timeline shown in Figure 1A.

Evaluation of EAMG model

To evaluate the EAMG mouse model, we included a total of four evaluation methods [55,56]. 1) Flip suspension test: Mice were placed on the cage top, which was then inverted and suspended above the home cage. The hanging time until each mouse fell was recorded, with a maximum cutoff of 600 s. Three measurements were taken per mouse, and the average was used for statistical analysis. 2) Clinical scoring using the Lennon grading method: grade 0, normal muscle strength and no muscle weakness, even after exercise; grade 1, normal at rest but weak after exercise, with chin on the floor and inability to raise head, hunched back, and reduced mobility; grade 2, grade 1 weakness at rest; grade 3, severe weakness, dehydrated, paralyzed (quadriplegic), and significant weight

loss. 3) Detection of serum CHRN-ab titer: Blood samples were collected via retro-orbital bleeding. Serum was separated and stored at −80°C. CHRN-ab levels were quantified by ELISA using peptide $CHRNA_{146–162}$ (1 μg/well) as the coating antigen. HRP-conjugated anti-mouse IgG (Jackson ImmunoResearch Laboratories, 115-035-003; 1:10000) was used for detection, with TMB substrate (Beyotime, P0209) for color development. The reaction was then stopped with the corresponding stop solution (Beyotime, P0215). 4) Electromyography: CMAP in mouse GAS muscles was recorded using low-frequency repetitive nerve stimulation (3 Hz).

Protein extraction and fractionation

Skeletal muscles (GAS and TA muscles) or cells were lysed in Triton X-100 buffer (1% Triton X-100 (Beyotime, ST1723), 20 mM Tris pH 7.5, 150 mM NaCl, 2 mM EDTA) supplemented with protease (Roche, 11697498001) and phosphatase (Roche, 4906845001) inhibitors. Homogenates were centrifuged at 20,000 × g for 15 min at 4°C to separate soluble (supernatant) and insoluble (pellet) fractions. The pellet was resuspended in urea lysis buffer containing 8 M urea (Sangon, A610148), 50 mM Tris pH 8.0, 100 mM NaCl, and 1% Triton X-100, supplemented with protease and phosphatase inhibitors and 10 mM DTT, and then sonicated (40% output power, 3 cycles of 10 s with a 30 s rest in between, with a pulse setting of 1 s on and 1 s off).

Cell culture, transfection, and pharmacological treatments

C2C12 and HEK293T cells were cultured in Dulbecco's modified Eagle's medium (Gibco, C11995500BT) supplemented with 10% fetal bovine serum and 1% penicillin-streptomycin (Gibco, 15140122) in a 5% CO_2 incubator. When the C2C12 cells reached approximately 80% confluence, the medium was replaced with differentiation medium, consisting of DMEM medium supplemented with 2% horse serum (Sangon, E510006), to induce myotube differentiation for 4–5 days. For transfection, RAPSN-MYC (G21275), RAPSN-mCherry (G35038), CHRNA-GFP (G65911), CHRNB/AChRβ-GFP (G65912), HSPA-Flag (G54460), BAG3-Flag (P5806), and LAMP2-EGFP (G57892) plasmids were obtained from MiaoLing. For knockdown of BAG3, HSPA and LAMP2A in C2C12 myotubes, siRNA was obtained from GeneChem. Transient transfections were performed using Lipofectamine 3000 Transfection Reagent (Invitrogen, L3000015) for plasmid and Rfect Transfection Reagent (Biodai, 11012) for siRNA, according to the manufacturer's protocol. For pharmacological treatments, cycloheximide (MedChemExpress, HY-12320; CHX), chloroquine (Selleck Chemicals, S6999; CQ), rapamycin (Selleck Chemicals, S1039; Rapa), MG132 (MedChemExpress, HY-13259), vinblastine (MedChemExpress, HY-13780), 3-methyladenine (Sigma-Aldrich, M9281; 3-MA), JG-98 (MedChemExpress, HY-117282), and TRC051384 (Selleck Chemicals, S8305; TRC) were dissolved according to the manufacturers' instructions.

Induction of CHRN clustering by agrin treatment or laminin coating

Two methods were used to induce CHRN clustering. In the agrin-based method, differentiated C2C12 myotubes were treated with recombinant rat agrin (R&D Systems, 550-AG) at 10 ng/mL in differentiation medium for 18 h. In the laminin-based method, culture dishes were coated with a thin layer of matrigel matrix (Corning, 356234), diluted to a working concentration of 100 μg/mL in cold serum-free DMEM. For 24-well plates, 500 μL of the solution was added per well. After incubation at 37°C for 1 h to allow gel polymerization, fresh medium was gently overlaid, and C2C12 myoblasts were subsequently seeded onto the coated surface and allowed to differentiate into myotubes.

Induction of CHRN internalization, and isolation of surface CHRN and its associated proteins

Myotubes were stimulated with agrin for 18 h, and incubated live with CHRN-ab (5 μg/mL) or control mouse IgG for 1 h at 4°C. Unbound antibodies were removed by washing with PBS (Sangon, E607008), and CHRN internalization was subsequently induced by shifting the cells to 37°C for 1 h. For the isolation of surface CHRN and its binding proteins, biotin-αBTX was prepared by reacting αBTX (Invitrogen, B1601) with biotin (Thermo Fisher Scientific, A39257), followed by purification using Zeba spin desalting columns (Thermo Fisher Scientific, 89883). As described previously [20], the cells were labeled with 300 nM biotin-αBTX for 2 h at 4°C, while unlabeled αBTX served as a negative control for streptavidin affinity isolation. After washing, cells were lysed in the extraction buffer containing 1% Thesit (Beyotime, ST736), 50 mM KCl, 2 mM $CaCl_2$, 4 mM $MgCl_2$, 20% glycerol, 50 mM Tris-HCl, and inhibitors of proteases and phosphatases (pH 7.4). Lysates were incubated with streptavidin-coupled dynabeads (Thermo Fisher Scientific, 65801D) for 20 min at 4°C and washed extensively with the extraction buffer except that the concentration of Thesit was 0.2%. Bead-associated proteins were resolved by SDS-PAGE.

Immunoblotting and co-immunoprecipitation assay

Proteins (10–20 μg) were separated by SDS-PAGE and transferred onto PVDF membranes (Merck Millipore, IPVH00010). Nonspecific binding was blocked with 5% skim milk diluted in 1X TBS (Servicebio, G0001) supplemented with Tween 20 0.1% (Sangon, A443678; TBST), and membranes were incubated with primary antibodies. After washing with TBST, membranes were incubated with HRP-conjugated secondary antibodies. After additional washes, signals were revealed using ECL substrate reagents (Thermo Fisher Scientific, 32106) and captured by chemiluminescent imaging system (Tanon). Quantifications were performed with ImageJ (National Institutes of Health) software. For co-immunoprecipitation assay, cell lysates were cleared by centrifugation at 12,000 × g for 10 min and incubated with the indicated antibodies overnight at 4°C, followed by incubation with Protein A/G PLUS agarose (Santa Cruz Biotechnology,

Table 1. Antibodies table.

Antibody name	Type	Dilution Immunostaining	Western blotting	Provider
RAPSN/rapsyn (1234)	Mouse Monoclonal	1:200		Invitrogen, MA1-746
RAPSN/rapsyn (1234)	Mouse Monoclonal		1:1,000	Santa Cruz Biotechnology, sc-58585
CHRNA1/AChRα1 (153)	Rat Monoclonal		1:1,000	Santa Cruz Biotechnology, sc-65829
HSPA/HSP70	Rabbit Polyclonal	1:200	1:2,000/CO-IP	Proteintech, 10,995-1-AP
BAG3	Rabbit Polyclonal	1:200	1:5,000	Proteintech, 10,599-1-AP
MAP1LC3A/B (D3U4C)	Rabbit Monoclonal		1:1,000	Cell Signaling Technology, 12,741
SQSTM1 (EPR4844)	Rabbit Monoclonal		1:1,000	Abcam, ab109012
LAMP2A	Rabbit Monoclonal		1:1,000	Abcam, ab125068
EEA1	Rabbit Polyclonal	1:250		Abcam, ab109110
RAB5	Rabbit Polyclonal	1:200		Abcam, ab18211
RAB7	Rabbit Monoclonal	1:200		Cell Signaling Technology, 9367
VIM/vimentin	Mouse Monoclonal	1:200		Santa Cruz Biotechnology, sc-6260
TUBA/α-tubulin	Rabbit Monoclonal	1:500		Abcam, ab52866
TUBA/α-tubulin	Rabbit Polyclonal		CO-IP	Proteintech, 11,224-1-AP
FLNC	Rabbit Polyclonal		1:1000	ABclonal, A13018
ACTN/α-actinin	Mouse Monoclonal	1:200		Sigma-Aldrich, A7811
MYC tag	Rabbit Polyclonal		1:1,000	Proteintech, 16,286-1-AP
FLAG tag	Mouse Monoclonal		1:5,000	Proteintech, 66,008-4-Ig
Normal Mouse IgG	Mouse Polyclonal			Sigma-Aldrich, 12-371
Normal Rabbit IgG	Rabbit Polyclonal			Cell Signaling Technology, 2729
Rabbit IgG Light Chain (HRP)	Monoclonal Mouse		1:5,000	Proteintech, SA00001-7 L
Rat IgG (HRP)	Goat Polyclonal		1:10,000	Cell Signaling Technology, 7077
Rabbit IgG (HRP)	Goat Polyclonal		1:10,000	Cell Signaling Technology, 7074
ACTB/β-actin (HRP)	Mouse Monoclonal		1:10,000	KangChen, KC-5A08
GAPDH	Mouse Monoclonal		1:1,000	Beyotime, AF0006

sc-2003) for 2 h at 4°C. Bound proteins were eluted and analyzed by immunoblotting. The antibodies used are listed in Table 1.

Immunofluorescence microscopy and image acquisition

C2C12 cells were washed with PBS and fixed with 4% paraformaldehyde for 10 min at room temperature. For experiments labeling CHRN clusters alone, fixed cells were incubated with αBTX-A594 (Invitrogen, B13423) or αBTX-A488 (Invitrogen, B13422) (1:1,000) for 1 h at room temperature. For co-staining experiments, after fixation, cells were permeabilized with 0.2% Triton X-100 in PBS for 10 min and blocked with 5% normal goat serum (Beyotime, C0265) for 1 h at room temperature, followed by incubation with the indicated primary antibodies overnight at 4°C. On the second day, after four washes with PBS, cells were incubated with appropriate secondary antibodies and/or αBTX-A594 or αBTX-A488 for 1 h at room temperature.

For skeletal muscles, tissues were embedded in Tissue-Tek OCT compound (Servicebio, G6059) and frozen in isopentane cooled with liquid nitrogen for cryostat sectioning (10-μm thick). TA muscle fibers were dissected, enzymatically dissociated with 1.5 mg/mL collagenase I (Sigma-Aldrich, C1-BIOC) for 45 min at 37°C, and subjected to mechanical dissociation to fiber tufts as described previously [57]. The diaphragm muscles were harvested intact and cleared of surrounding connective tissue. All muscle samples were fixed in 4% paraformaldehyde for 30 min at room temperature, and incubated with either αBTX-A594 or αBTX-A488 for 1 h, or permeabilized with 1% Triton X-100 for 30 min at room temperature and then incubated with specific primary and secondary antibodies for immunostaining. The antibodies used are listed in Table 1.

Sequential labeling of CHRN in live myotubes

Four-day-old C2C12 myotubes were treated with agrin for 18 h to induce CHRN clustering. Preexisting surface CHRN was first labeled with αBTX-A488 (1:1000) for 1 h at room temperature, followed by incubation with a saturating concentration of unlabeled αBTX (6 μM, 30 min) to block residual binding sites. Cells were then incubated with CHRN-ab (5 μg/mL) or control mouse IgG for 1 h at 4°C and then shifted to 37°C in a cell culture incubator for 12 h to induce CHRN internalization and allow synthesis and membrane insertion of newly synthesized CHRN. Newly inserted surface CHRN was then labeled with αBTX-A594 (1:500) for 1 h. Imaging was performed at two time points, before internalization ($T = 0$ h, after blocking) and after labeling of newly inserted CHRN ($T = 13$ h). The same fields were imaged to track preexisting (green) and newly inserted (red) CHRN. For quantification, regions of interest (ROIs) were defined based on CHRN clusters identified at $T = 0$ h. The areas of remaining preexisting CHRN and newly inserted CHRN within the same ROIs at $T = 13$ h were measured using ImageJ. Data were expressed as the percentage of the $T = 0$ h CHRN cluster area (baseline).

CHRN cluster quantitative immunofluorescence analysis

Images were acquired randomly using TCS SP8 confocal microscope (Leica Microsystems) with either a HC PL APO CS2 63 × 1.4 NA oil or a 40 × 1.25 NA objective or UPLFLN 40X, 0.75 NA, WD 0.51 mm (Olympus) microscope. For CHRN cluster analysis in C2C12 myotubes, images were acquired as single optical sections. A consistent threshold was applied across all images using ImageJ software, which was adjusted for the binary image so that it matched the pattern of CHRN clusters that was

perceived by eye. CHRN clusters with an area equal to or greater than 4 μm^2 were included for analysis. For accurate analysis of skeletal muscle samples, each image was captured on en-face NMJs. NMJs were generated by collecting a z-stack of 3–15 images with focal planes 0.15 μm apart and collapsed into a single projection per field of view. SP8 deconvolution was carried out with HyVolution. Image acquisition and analyses were performed in a blinded manner. At least three images per group were selected for quantification. Quantification of puncta number and size, and colocalization events of the acquired images was performed using ImageJ software.

RNA extraction, reverse transcription, and PCR

Total RNA was extracted using TRI reagent (Sigma-Aldrich, T9424). Reverse transcription was performed using HiScript II Q RT SuperMix for qPCR (Vazyme, R223-01). Quantitative PCR analysis was performed on a Light Cycler 96 Real-Time System for 45 cycles using a SYBR qPCR Master Mix (Vazyme, Q712-02). The relative transcription levels of target genes were calculated by the $2^{-\Delta\Delta Ct}$ method. Primers were designed with Primer 3 software from gene sequences obtained from GenBank. Primer specificity was determined using a BLAST search. The primer pairs used for qPCR were as follows: *Hspa1a* (F: GCACAAGCGGGAGGAGC, R: CAGAGGCTCCTTTCGGCG), *Hspa8* (F: CCAAGGTCCAAGTGGAATACAAA, R: CTTTCCGAGGTACGCTTCTG), *Hsp90ab1* (F: GTCCGCCGTGTGTTCATCAT, R: GCACTTCTTGACGATGTTCTTGC), *Rapsn* (F: TTTGCCGTGGTCCAGATTGAT, R: CAGGTTCAGGTAGCTTTCGAG), *Gapdh* (F: AGGTCGGTGTGAACGGATTTG, R: TGTAGACCATGTAGTTGAGGTCA).

Establishment of HSPA knockdown and inhibition models in EAMG

After the initial immunization, EAMG mice were randomly assigned to control and HSPA knockdown groups. Mice in the respective groups received in situ intramuscular injections of either AAV carrying a non-targeting control sequence (AAV9-EGFP) or an *Hspa1a*-specific short hairpin RNA construct (AAV9-*Hspa1a* shRNA-EGFP) (GeneChem). The virus was injected bilaterally into GAS muscles at five points (4 μL/point), with a total viral load of 1×10^{11} vector genomes (v.g.) per leg. One month post-injection, viral transduction efficiency in the GAS muscles was assessed by *in vivo* fluorescence imaging using an IVIS Spectrum Small Animal Live Imaging System (PerkinElmer) to detect the EGFP signal. The acquired images were quantitatively analyzed by defining ROIs. For the pharmacological inhibition of HSPA, EAMG mice received intraperitoneal injections of JG-98 (1 mg/kg). The treatment was administered every other day for two weeks, starting from the third immunization.

Statistical analysis

All statistical analyses were performed using GraphPad Prism 10.1 software. Data were presented as means ± SEM. Comparisons between two groups were made by unpaired Student's t-test if the data followed a normal distribution. Otherwise, the nonparametric Mann-Whitney U test was applied. For comparison of more than two groups, one-way or two-way ANOVA was performed as annotated in the figure legends. When ANOVA was significant, Bonferroni post hoc test was used for multiple comparisons. $p < 0.05$ was considered statistically significant.

Acknowledgements

We would like to thank Xiaoyun Huang from Huashan Hospital Affiliated to Fudan University for his technical assistance on the electromyography.

Author contributions

CRediT: **Yujia Liu:** Formal analysis, Investigation, Methodology, Writing – original draft; **Guofang Xia:** Data curation, Writing – review & editing; **Huaiying Shi:** Data curation, Formal analysis; **Simeng Zhu:** Resources; **Hailong Li:** Methodology; **Yifan Shi:** Formal analysis; **Wanling Ouyang:** Data curation; **Congfeng Xu:** Conceptualization, Funding acquisition, Resources, Supervision, Writing – review & editing; **Ailian Du:** Conceptualization, Funding acquisition, Resources, Supervision, Writing – review & editing.

Funding

The work was supported by the National Natural Science Foundation of China [82171812, 81971181]; Medical and Engineering Crossover Fund of Shanghai Jiao Tong University [YG2024ZD27].

Disclosure statement

No potential conflict of interest was reported by the author(s).

Data availability statement

The data that support the findings of this study are available on request from the corresponding author.

ORCID

Congfeng Xu http://orcid.org/0000-0002-8009-4865

References

[1] Punga AR, Maddison P, Heckmann JM, et al. Epidemiology, diagnostics, and biomarkers of autoimmune neuromuscular junction disorders. Lancet Neurol. 2022;21(2):176–188. doi: 10.1016/s1474-4422(21)00297-0

[2] Iorio R. Myasthenia gravis: the changing treatment landscape in the era of molecular therapies. Nat Rev Neurol. 2024;20(2):84–98. doi: 10.1038/s41582-023-00916-w

[3] Kaminski HJ, Sikorski P, Coronel SI, et al. Myasthenia gravis: the future is here. J Clin Invest. 2024;134(12):e179742. doi: 10.1172/JCI179742

[4] Du A, Huang S, Zhao X, et al. Suppression of CHRN endocytosis by carbonic anhydrase CAR3 in the pathogenesis of myasthenia

gravis. Autophagy. 2017;13(11):1981–1994. doi: 10.1080/15548627.2017.1375633
[5] Christadoss P, Lindstrom J, Munro S, et al. Muscle acetylcholine receptor loss in murine experimental autoimmune myasthenia gravis: correlated with cellular, humoral and clinical responses. J Neuroimmunol. 1985;8(1):29–41. doi: 10.1016/s0165-5728(85)80045-x
[6] Fambrough DM, Drachman DB, Satyamurti S. Neuromuscular junction in myasthenia gravis: decreased acetylcholine receptors. Science. 1973;182(4109):293–295. doi: 10.1126/science.182.4109.293
[7] Fichtner ML, Horstkorte L, Sánchez Navarro BG, et al. Autoantibodies in myasthenia gravis. Int Rev Neurobiol. 2025;182:89–119. doi: 10.1016/bs.irn.2025.04.024
[8] Fertuck HC, Salpeter MM. Quantitation of junctional and extrajunctional acetylcholine receptors by electron microscope autoradiography after 125i-alpha-bungarotoxin binding at mouse neuromuscular junctions. J Cell Biol. 1976;69(1):144–158. doi: 10.1083/jcb.69.1.144
[9] Herbst R, Huijbers MG, Oury J, et al. Building, breaking, and repairing neuromuscular synapses. Cold Spring Harb Perspect Biol. 2024;16(5):a041490. doi: 10.1101/cshperspect.a041490
[10] Li L, Cao Y, Wu H, et al. Enzymatic activity of the scaffold protein rapsyn for synapse formation. Neuron. 2016;92(5):1007–1019. doi: 10.1016/j.neuron.2016.10.023
[11] Xing G, Jing H, Zhang L, et al. A mechanism in agrin signaling revealed by a prevalent rapsyn mutation in congenital myasthenic syndrome. Elife. 2019;8:e49180. doi: 10.7554/eLife.49180
[12] Frail DE, McLaughlin LL, Mudd J, et al. Identification of the mouse muscle 43,000-dalton acetylcholine receptor-associated protein (RAPsyn) by cDNA cloning. J Biol Chem. 1988;263(30):15602–15607. doi: 10.1016/S0021-9258(19)37631-8
[13] Xing G, Xiong WC, Mei L. Rapsyn as a signaling and scaffolding molecule in neuromuscular junction formation and maintenance. Neurosci Lett. 2020;731:135013. doi: 10.1016/j.neulet.2020.135013
[14] Marchand S, Bignami F, Stetzkowski-Marden F, et al. The myristoylated protein rapsyn is cotargeted with the nicotinic acetylcholine receptor to the postsynaptic membrane via the exocytic pathway. J Neurosci. 2000;20(2):521–528. doi: 10.1523/jneurosci.20-02-00521.2000
[15] Marchand S, Devillers-Thiéry A, Pons S, et al. Rapsyn escorts the nicotinic acetylcholine receptor along the exocytic pathway via association with lipid rafts. J Neurosci. 2002;22(20):8891–8901. doi: 10.1523/jneurosci.22-20-08891.2002
[16] Han H, Yang SH, Phillips WD. Overexpression of rapsyn modifies the intracellular trafficking of acetylcholine receptors. J Neurosci Res. 2000;60(2):155–163. doi: 10.1002/(SICI)1097-4547(20000415)60:2<155::AID-JNR4>3.0.CO;2-N
[17] Xing G, Jing H, Yu Z, et al. Membraneless condensates by Rapsn phase separation as a platform for neuromuscular junction formation. Neuron. 2021;109(12):1963–1978.e1965. doi: 10.1016/j.neuron.2021.04.021
[18] Aittaleb M, Chen PJ, Akaaboune M. Failure of lysosome clustering and positioning in the juxtanuclear region in cells deficient in rapsyn. J Cell Sci. 2015;128(20):3744–3756. doi: 10.1242/jcs.172536
[19] Chen PJ, Martinez-Pena YVI, Aittaleb M, et al. AChRs are essential for the targeting of rapsyn to the postsynaptic membrane of NMJs in living mice. J Neurosci. 2016;36(21):5680–5685. doi: 10.1523/jneurosci.4580-15.2016
[20] Luo S, Zhang B, Dong XP, et al. Hsp90 beta regulates rapsyn turnover and subsequent AChR cluster formation and maintenance. Neuron. 2008;60(1):97–110. doi: 10.1016/j.neuron.2008.08.013
[21] Bauer B, Martens S, Ferrari L. Aggrephagy at a glance. J Cell Sci. 2023;136(10). doi: 10.1242/jcs.260888
[22] Lamark T, Johansen T. Aggrephagy: selective disposal of protein aggregates by macroautophagy. Int J Cell Biol. 2012;2012:736905. doi: 10.1155/2012/736905
[23] Ma X, Lu C, Chen Y, et al. Cct2 is an aggrephagy receptor for clearance of solid protein aggregates. Cell. 2022;185(8):1325–1345.e1322. doi: 10.1016/j.cell.2022.03.005
[24] Zhou J, Chuang Y, Redding-Ochoa J, et al. The autophagy adaptor TRIAD3A promotes tau fibrillation by nested phase separation. Nat Cell Biol. 2024;26(8):1274–1286. doi: 10.1038/s41556-024-01461-4
[25] Tedesco B, Vendredy L, Timmerman V, et al. The chaperone-assisted selective autophagy complex dynamics and dysfunctions. Autophagy. 2023;19(6):1619–1641. doi: 10.1080/15548627.2022.2160564
[26] Klimek C, Kathage B, Wördehoff J, et al. Bag3-mediated proteostasis at a glance. J Cell Sci. 2017;130(17):2781–2788. doi: 10.1242/jcs.203679
[27] Gamerdinger M, Hajieva P, Kaya AM, et al. Protein quality control during aging involves recruitment of the macroautophagy pathway by BAG3. Embo J. 2009;28(7):889–901. doi: 10.1038/emboj.2009.29
[28] Arndt V, Dick N, Tawo R, et al. Chaperone-assisted selective autophagy is essential for muscle maintenance. Curr Biol. 2010;20(2):143–148. doi: 10.1016/j.cub.2009.11.022
[29] Meister-Broekema M, Freilich R, Jagadeesan C, et al. Myopathy associated BAG3 mutations lead to protein aggregation by stalling Hsp70 networks. Nat Commun. 2018;9(1):5342. doi: 10.1038/s41467-018-07718-5
[30] Gibertini S, Ruggieri A, Cheli M, et al. Protein aggregates and aggrephagy in myopathies. Int J Mol Sci. 2023;24(9):8456. doi: 10.3390/ijms24098456
[31] Bruneau EG, Brenner DS, Kuwada JY, et al. Acetylcholine receptor clustering is required for the accumulation and maintenance of scaffolding proteins. Curr Biol. 2008;18(2):109–115. doi: 10.1016/j.cub.2007.12.029
[32] Rudolf R, Straka T. Nicotinic acetylcholine receptor at vertebrate motor endplates: endocytosis, recycling, and degradation. Neurosci Lett. 2019;711:134434. doi: 10.1016/j.neulet.2019.134434
[33] Chong SH, Ham S. Distinct role of hydration water in protein misfolding and aggregation revealed by fluctuating thermodynamics analysis. Acc Chem Res. 2015;48(4):956–965. doi: 10.1021/acs.accounts.5b00032
[34] Bokvist M, Lindström F, Watts A, et al. Two types of Alzheimer's beta-amyloid (1–40) peptide membrane interactions: aggregation preventing transmembrane anchoring versus accelerated surface fibril formation. J Mol Biol. 2004;335(4):1039–1049. doi: 10.1016/j.jmb.2003.11.046
[35] Lee J, Chin N, Zou J, et al. Chip protects lysosomes from CLN4 mutant-induced membrane damage. Nat Cell Biol. 2025;27(9):1465–1481. doi: 10.1038/s41556-025-01738-2
[36] Men Y, Hirayama S, Ao S, et al. Escrt-I and Ptpn23 mediate microautophagy of ubiquitylated tau aggregates. J Cell Biol. 2025;224(6). doi: 10.1083/jcb.202406120
[37] Mohanan A, Deshpande S, Jamadarkhana PG, et al. Delayed intervention in experimental stroke with TRC051384–a small molecule HSP70 inducer. Neuropharmacology. 2011;60(6):991–999. doi: 10.1016/j.neuropharm.2010.12.003
[38] Li X, Colvin T, Rauch JN, et al. Validation of the Hsp70-Bag3 protein-protein interaction as a potential therapeutic target in cancer. Mol Cancer Ther. 2015;14(3):642–648. doi: 10.1158/1535-7163.Mct-14-0650
[39] Nassar M, Samaha H, Ghabriel M, et al. Lc3a silencing hinders aggresome vimentin cage clearance in primary choroid plexus carcinoma. Sci Rep. 2017;7(1):8022. doi: 10.1038/s41598-017-07403-5
[40] Gamerdinger M, Kaya AM, Wolfrum U, et al. Bag3 mediates chaperone-based aggresome-targeting and selective autophagy of misfolded proteins. EMBO Rep. 2011;12(2):149–156. doi: 10.1038/embor.2010.203
[41] Ohno K, Engel AG, Shen XM, et al. Rapsyn mutations in humans cause endplate acetylcholine-receptor deficiency and myasthenic syndrome. Am J Hum Genet. 2002;70(4):875–885. doi: 10.1086/339465

[42] Phillips WD, Vladeta D, Han H, et al. Rapsyn and agrin slow the metabolic degradation of the acetylcholine receptor. Mol Cell Neurosci. 1997;10(1–2):16–26. doi: 10.1006/mcne.1997.0634
[43] Martínez-Martínez P, Phernambucq M, Steinbusch L, et al. Silencing rapsyn in vivo decreases acetylcholine receptors and augments sodium channels and secondary postsynaptic membrane folding. Neurobiol Dis. 2009;35(1):14–23. doi: 10.1016/j.nbd.2009.03.008
[44] Mogk A, Bukau B, Kampinga HH. Cellular handling of protein aggregates by disaggregation machines. Mol Cell. 2018;69(2):214–226. doi: 10.1016/j.molcel.2018.01.004
[45] Park JY, Ikeda H, Ikenaga T, et al. Acetylcholine receptors enable the transport of rapsyn from the Golgi complex to the plasma membrane. J Neurosci. 2012;32(21):7356–7363. doi: 10.1523/jneurosci.0397-12.2012
[46] Bruneau E, Akaaboune M. The dynamics of the rapsyn scaffolding protein at individual acetylcholine receptor clusters. J Biol Chem. 2007;282(13):9932–9940. doi: 10.1074/jbc.M608714200
[47] Pratt WB, Morishima Y, Peng HM, et al. Proposal for a role of the Hsp90/Hsp70-based chaperone machinery in making triage decisions when proteins undergo oxidative and toxic damage. Exp Biol Med (Maywood). 2010;235(3):278–289. doi: 10.1258/ebm.2009.009250
[48] Morán Luengo T, Mayer MP, Rüdiger SGD. The Hsp70-Hsp90 chaperone cascade in protein folding. Trends Cell Biol. 2019;29(2):164–177. doi: 10.1016/j.tcb.2018.10.004
[49] Mylvaganam S, Earnshaw R, Heymann G, et al. C-terminus of Hsp70 interacting protein (CHIP) and neurodegeneration: lessons from the bench and bedside. Curr Neuropharmacol. 2021;19(7):1038–1068. doi: 10.2174/1570159x18666201116145507
[50] Heck JW, Cheung SK, Hampton RY. Cytoplasmic protein quality control degradation mediated by parallel actions of the E3 ubiquitin ligases Ubr1 and San1. Proc Natl Acad Sci USA. 2010;107(3):1106–1111. doi: 10.1073/pnas.0910591107
[51] Pei J, Wen C, You Q, et al. Small molecules targeting HSP70 and therapeutic potentials. Eur J Med Chem. 2026;303:118402. doi: 10.1016/j.ejmech.2025.118402
[52] Iwasa K, Nambu Y, Motozaki Y, et al. Increased skeletal muscle expression of the endoplasmic reticulum chaperone GRP78 in patients with myasthenia gravis. J Neuroimmunol. 2014;273(1–2):72–76. doi: 10.1016/j.jneuroim.2014.05.006
[53] Du A, Huang S, Zhao X, et al. Endoplasmic reticulum stress contributes to acetylcholine receptor degradation by promoting endocytosis in skeletal muscle cells. J Neuroimmunol. 2016;290:109–114. doi: 10.1016/j.jneuroim.2015.11.024
[54] Ryu SW, Stewart R, Pectol DC, et al. Proteome-wide identification of HSP70/HSC70 chaperone clients in human cells. PLOS Biol. 2020;18(7):e3000606. doi: 10.1371/journal.pbio.3000606
[55] Tuzun E, Berrih-Aknin S, Brenner T, et al. Guidelines for standard preclinical experiments in the mouse model of myasthenia gravis induced by acetylcholine receptor immunization. Exp Neurol. 2015;270:11–17. doi: 10.1016/j.expneurol.2015.02.009
[56] Wu B, Goluszko E, Huda R, et al. Experimental autoimmune myasthenia gravis in the mouse. Curr Protoc Immunol. 2013;100(1). doi: 10.1002/0471142735.im1508s100
[57] Osseni A, Sébastien M, Sarrault O, et al. Triadin and CLIMP-63 form a link between triads and microtubules in muscle cells. J Cell Sci. 2016;129(20):3744–3755. doi: 10.1242/jcs.188862